INDUCTIVE ACTIVATION OF MAGNETITE FILLED SHAPE MEMORY POLYMERS

A Thesis
Presented to
The Academic Faculty

by

Greg Vialle

In Partial Fulfillment
of the Requirements for the Degree
Master of Science in the
School of Materials Science and Engineering

Georgia Institute of Technology
April 2009

INDUCTIVE ACTIVATION OF MAGNETITE FILLED SHAPE MEMORY POLYMER

Approved by:

Dr. Hamid Garmestani, Advisor
School of Materials Science and Engineering
Georgia Institute of Technology

Dr. Ken Gall
School of School of Materials Science and Engineering
Georgia Institute of Technology

Dr. Naresh Thadhani
School of School of Materials Science and Engineering
Georgia Institute of Technology

Date Approved: 3 April 2009

To my son, Alex.

ACKNOWLEDGEMENTS

I wish to thank my wife, who, while I gestated this thesis, was bearing a much greater creation, and got it right the first time. I'd like to thank Professor Ian Ferguson for the use of his VSM equipment, and Professor CP Wong for use of his Impedance Analyzer. Many thanks go to Matthew Di Prima for assistance with all aspects of foam processing and thermomechanical characterization. This research was funded through a university research grant by Raytheon Missile Systems and through the Air Force Research Laboratory with a Phase 2 STTR.

TABLE OF CONTENTS

LIST OF TABLES

LIST OF FIGURES

LIST OF SYMBOLS AND ABBREVIATIONS

A	Ampere units
A_s	Surface Area
B	Magnetic Flux Density
B_r	Remanance
B_s	Saturation
G	Gauss units
H	Applied Magnetic Field
H_c	Coercivity
L	Inductance
M	Magnetic response/Magnetization
M_r	Remanent Magnetization
M_s	Saturation Magnetization
N	Number of Turns or Shape Factor
r	Radius
R	Electrical Resistance
$\mathcal{R}$	MagneticReluctance
T	Tesla units
V	Electric Potential or Voltage units
V	Volume
W_h	Hysteresis work
Φ	Magnetic Flux
μ	Magnetic Permeability
μ_r	Relative Magnetic Permeability

μ_o	Magnetic Permeability of Free Space
ρ	Density
AC	Alternating Current
DC	Direct Current
EMI	Electromagnetic Interference
mmf	magnetomotive force
RF	Radio Frequency
VSM	Vibrating Sample Magnetometer

SUMMARY

Thermally activated shape memory polymers are a desirable material for use in dynamic structures due to their large strain recovery, light weight, and tunable activation. The addition of ferromagnetic susceptor particles to a polymer matrix provides the ability to heat volumetrically and remotely via induction. Here, remote induction heating of magnetite filler particles dispersed in a thermoset matrix is used to activate shape memory polymer as both solid and foam composites. Bulk material properties and performance are characterized and compared over a range of filler parameters, induction parameters, and packaging configurations. Magnetite filler particles are investigated over a range of power input, in order to understand the effects of particle size and shape on heat generation and flux into the matrix. This investigation successfully activates shape memory polymers in 10 to 20 seconds, with no significant impact of filler particles up to 10wt% on mechanical properties of shape memory foam. Performance of different particle materials is dependent upon the amplitude of the driving magnetic field. There is a general improvement in heating performance for increased content of filler particles. Characterization indicates that heat transfer between the filler nanoparticles and the foam is the primary constraint in improved heating performance. The use of smaller, acicular particles as one way to improve heat transfer, by increasing interfacial area between filler and matrix, is further examined.

CHAPTER 1:

INTRODUCTION

Overview of Induction Heated SMP Activation

Shape memory polymers (SMPs) are smart materials designed to undergo changes in stiffness in response to a stimulus. These changes in stiffness lead to macroscopic strain recovery. The most common stimulus for SMP materials is heat. Thermal activation is traditionally achieved through the transfer of thermal energy from the environment directly into the sample through its surface via conduction, convection or thermal radiation[1-4]. Such surface mediated heat transfer mechanisms inherently have both physical constraints and design implications.

Many physical constraints arise from part geometry: surface area constrains the heat flux from the environment in surface mediated heat transfer. The resulting thermal gradients can contribute to non-uniform activation, and activation speed is limited by the diffusion of heat from the surface to the central regions of the part. Polymers are not noted for high thermal conductivity[5].

Design limitations, such as when thermal isolation of the part is required, can also constrain thermal activation of SMP material. Biomedical stents are one example of such a design constrained application, requiring remote activation of the in vivo SMP material without significant heating of surrounding tissue[6].

Some of these physical and design constraints can be overcome through induction heating, which can be done remotely and heats volumetrically. Traditional isothermal surface

mediated heating can activate SMPs on the order of minutes to tens of minutes dependent on the activation temperature of the material[7, 8]; remote light activated SMPs require a 20 minute laser warm up and 15 minute recovery[9]. By contrast, remotely heated induction times have been reported in the 15-25 second range[6, 10].

In addition to challenges with environmental thermal activation stimuli, certain applications of shape memory polymers demand anisotropic shape changes often difficult to achieve with solid materials. For example, smart aerospace structures may require a uniaxial shape change with minimal transverse deformation in order to maintain an aerodynamic surface profile[11, 12]. SMP based foams offer a potential solution to the anisotropic strain recovery demand in structures, and allow for an optimized trade-off between weight and mechanical properties for a given application by tuning the relative density of the foam. However, foam structure can further limit the already poor heat conduction of the solid resin.

Objectives

This work explores the reinforcement of SMP solid resin composites and foams by ferromagnetic susceptor particles, which enables volumetric remote activation of the bulk material via induction. The first objective of this research is to demonstrate the viability of activating shape memory polymer foams via induction heating, and develop a methodology for evaluating performance. The second objective is to understand the effects of material (composite microstructure, particle size and shape), and system parameters (field strength) on heating performance.

Background

The overarching concept of induction heated SMP activation is illustrated in Figure 1: High frequency alternating current induces an alternating magnetic field of driving amplitude of H_D inside the coil. This alternating field induces an electromagnetic response in ferromagnetic susceptor particles dispersed within the resin matrix of a foam SMP sample. At high frequencies, the response incurs significant losses due to eddy currents (P_e) and hysteresis (P_h) which diffuse as thermal energy from the susceptor particles into the polymer matrix via conduction. As the polymer approaches its transition temperature (T_g), increased chain mobility allows the material to macroscopically transform to a rubbery state, resulting in a deformation recovery (ε_r) of the mechanically unconstrained foam. While still above T_g, the foam can be repackaged again by compressing and constraining it until it has cooled back down below T_g. Recovery performance for chemically cross linked networked polymers is not significantly affected by the number of cycles or by storage time[13].

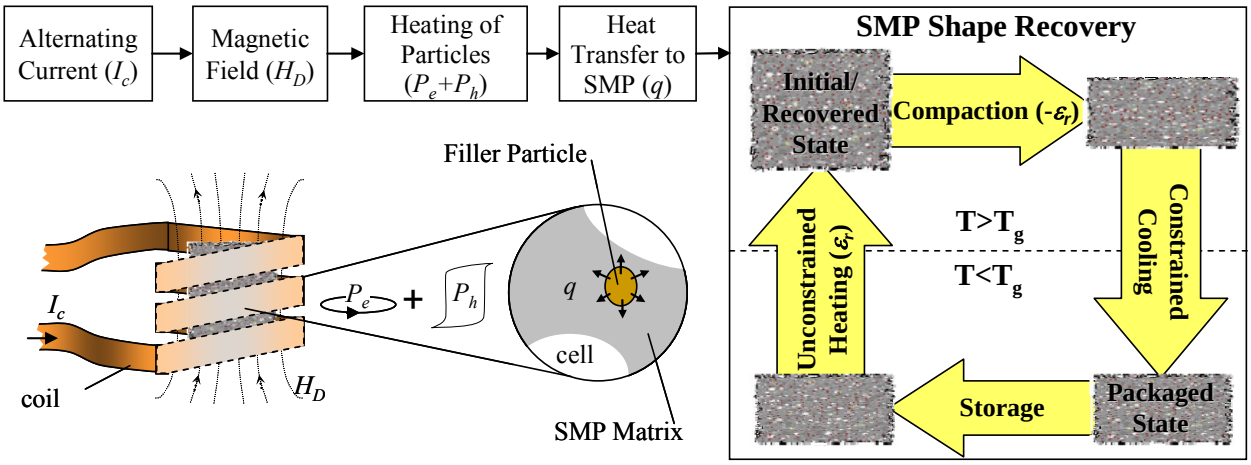

Figure 1.1: Theory of operation for inductively activated shape memory polymer

The following sections deconstruct the mechanisms and underlying theory of each step in more detail.

Electromagnetic (AC) Field Generation

Electricity is based upon the concept of electric charge. Current, *I*, measures the rate of charge flow in amps. Alternating current (AC) with a sinusoidal cycle of angular frequency $\omega=2\pi f$ is commonly used, and can be mathematically described in complex terms by Eq. 1 as a function of time, t, with a peak current I_o:

$$\widetilde{I} = I(t) = I_o e^{j\omega t} \tag{1}$$

Electric power is a scalar product of the electric potential, *V*, and the current, both of which vary with time. For a sinusoidal waveform, the time averaged power is based on the root mean square voltage, $V_{rms}=\sqrt{2}V_{peak}$.

$$P = I_o \cdot V_{rms} \tag{2}$$

The electric potential (voltage) is dependent upon the complex circuit impedance, Z^*. For an induction coil, there are two contributions to the impedance: coil resistance, *R*, and inductance, *L*.

$$V = Z^* \cdot I \tag{3}$$

$$Z^* = R + j\omega L \tag{4}$$

The inductance is determined by the coil geometry, and also by the magnetic properties of the material inside the coil. For a helical coil, the primary parameters are number of turns (*N*), height (*h*), and coil diameter (*d*), and the effective permeability (μ) inside the coil.

$$L = \mu N^2 \frac{\pi d^2}{4h} \tag{5}$$

Ampere's Law (Eq. 6) governs the generation of magnetic fields via electricity

$$\nabla \times H = \frac{dI}{dA} + \varepsilon \frac{\partial E}{\partial t} \tag{6}$$

where *dI/dA* is the current density through the coil ε is the permittivity of the core and *E* is the electric field[14].

Induction Heating

Induction heating uses high frequency (typically f >10 kHz) current to generate cyclic magnetic fields (H) via an induction coil. Magnetic induction causes eddy current (P_e) and hysteresis power losses (P_h) in the material located within the coil. The total thermal power generation of sample is the sum of those electromagnetic loss components:

$$\dot{q}_g = P_e + P_h \tag{7}$$

Eddy current heating occurs as a skin effect in the heated bulk sample, and relies upon Joule heating:

$$P_e = I^2 R_s \tag{8}$$

where R_s is the bulk resistance in the heated sample. However, if the electrical resistivity of the material is high enough, current will not flow, and the eddy current losses will be negligible. Such is the case for most polymers, so for this research the primary induction heating mechanism is expected to be hysteresis heating[15].

Hysteresis is a phenomenon describing the path dependent magnetic response of ferromagnetic materials to an applied magnetic field (Fig. 2). Subsequently, the hysteresis

heating mechanism is restricted to these materials, but is generated very locally, such that susceptor particles of small scale can be used to heat a bulk matrix of non-ferromagnetic material. Hysteresis heating per cycle is proportional to the area of the hysteresis loop created by the driving magnetic field (H_D) and the intrinsic induced magnetic response of the material (B_i).

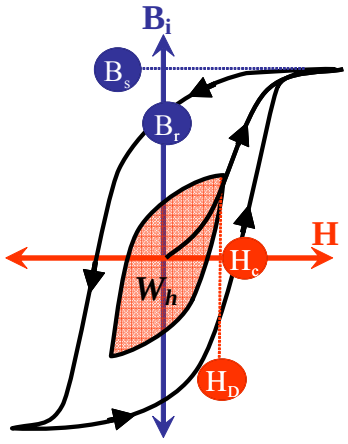

Figure 1.2: Typical hysteresis curve for a ferromagnetic material. Figure shows initial magnetization curve, minor (inner shaded area, W_h) and major (outer curve) hysteresis loops.

This thermal energy loss due to hysteresis can be estimated by computing the area inside the minor hysteresis loop and is given by[16]:

$$P_h = V \cdot W_h \cdot f \tag{9}$$

where V is the volume of the sample, W_h is the net magnetic work per cycle calculated from the area inside the B-H loop, and f is the frequency. Thus for high drive levels ($H_D \approx H_c$), hard magnetic materials, characterized by high remanence (B_r) and high coercivity (H_c), generate the most heat per cycle. In addition to being an inherent material property, coercivity is also a function of the particle size and shape [17]. Once the temperature exceeds the Curie temperature (T_c) of the filler material, the magnetic response behavior transitions from ferromagnetic to paramagnetic, self limiting the hysteresis heating to $T<T_c$.

Susceptor materials can be selected for a customized material design based upon the available field and heating requirements. Various susceptor materials selected for cost, magnetic response, and Curie temperature have been investigated. Nickel susceptor particles were the subject of research by Suwanwatana, et al, who investigated the effects of both particle size and volumetric loading in thermoplastic composite bonding polymers[18]. Working with biomedical applications, Buckley et al (2005) researched remote activation via induction of both solid and foam polyurethane SMP materials using nickel zinc ferrite susceptor particles, selected for low Curie temperature thermoregulation[6]. Razzaq, et al (2008), followed up on their previous work with magnetite filler and characterized some of the electrical and magnetic properties in addition to the mechanical effects in polyurethane SMPs[19, 20]. However, these prior works have not quantitatively addressed the effect of particle concentration on the shape packaging and recovery properties of SMPs, nor have they comprehensively addressed efficiency of induction heating from the electrical power source through to thermal activation of the material.

Particulate magnetite (Fe_3O_4) was selected as the susceptor reinforcement for this investigation due to its hard magnetic properties, and subsequent capacity for high hysteresis heat generation. Because magnetite is already an oxide, it also offers excellent chemical stability, even for nanoscale particles.

Heat Transfer

Heat transfer within the sample occurs primarily via the conduction mechanism from the susceptor particles to the matrix and is driven by temperature gradient as given by Fourier's Law:

$$\dot{q}_{cond} = -k \cdot A_p \nabla T \tag{10}$$

where A_p is the surface area of the particle, k is the intrinsic thermal conductivity of the matrix and $\dot{q}_{cond}$ is the heat flux through the particle matrix interface.

For the bulk sample, applying the energy flux balance in Eq. 11 yields Eq. 12 where A_s is the effective surface area of the sample (adjusted for geometry) and the *q"* terms are the heat flux due to radiation and convection, m is the particle mass and c_p is the specific heat capacity:

$$\dot{q}_{in} = \dot{q}_{out} + \dot{q}_{stored} \tag{11}$$

$$V\dot{q}_g = A_s\left(q''_{rad} + q''_{conv}\right) + mc_p\frac{dT}{dt} \tag{12}$$

The radiation and convection heat terms represent the heat lost to the surroundings through the surface, A_s and are respectively given by:

$$q''_{rad} = \varepsilon\sigma\left(T_s^4 - T_a^4\right) \tag{13}$$

$$q''_{conv} = h\left(T_s - T_a\right) \tag{14}$$

where ε is emissivity of the sample, σ is the Stefan-Boltzman constant (=5.67×10^{-8} W·m^{-2}K^{-4}), h is the convection heat transfer coefficient, and T_s and T_a are the respective temperatures of the sample surface and the ambient surroundings[5].

Shape Recovery

SMPs have the ability to undergo and recover large strains. In thermally activated cross linked polymers, the shape memory effect is entropic in nature. When heated near the glass transition temperature (T_g) the polymer chains can undergo rotational conformational changes, allowing the polymer chains to be uniaxially strained. As the material is strained, the alignment of the chains increases, which increases the stored energy in the material as the configurational entropy of the chain decreases. This energy is subsequently locked into the polymer chains when

the material is cooled below T_g and the chains are restricted from freely rotating via interactions with their neighbors. When the polymer is reheated above T_g without constraint, an increase of entropy serves as a driving force for the material to recover its initial shape [13].

Thermally activated SMPs can be synthesized as thermoplastic or thermoset materials. Thermoplastic SMPs are typically polyurethanes that use physical cross linking to drive the shape recovery process. They have finite shape memorization capability and often require mechanical training to insure full shape recovery[13, 21]. Tey (2000) and other researchers have independently investigated the thermomechanical properties of polyurethane SMPs[2]. Koerner, et al demonstrated remote (but still surface mediated) activation via infrared radiation using a carbon nanotube reinforced thermoplastic material[22]. To date, most of the work in remote SMP activation via induction has been with polyurethane materials.

On the other hand, thermoset epoxies rely on chemical cross links to enable the shape recovery process, have greater shape memorization capacity, and there is no requirement for mechanical training[13, 23-25]. Thermoset epoxies have been studied much less than polyurethanes, particularly with regard to induction heating. Gross and Weiland (2007) recently reported on the mechanical performance in morphing aircraft applications of a styrene based epoxy SMP[24]. Based on epoxy SMP foam, Sanderson, et al, investigated the thermal properties in surface heated scenarios, and highlighted the need for volumetric heating of this material for morphing aircraft applications[26].

CHAPTER 2: METHODS

Material Selection and Processing

Matrix

Commercially available shape memory polymer resin from Composite Technology Development, Inc. (CTD) was used for the matrix. DP5.1 is a two part thermoset epoxy with a cured density of 1.09 (g/cm^3). The nominal T_g for cured DP5.1 resin is 75°C, but can vary by several degrees, dependent on mixing ratio, curing temperature, and fillers.

Susceptor Particles

Magnetite was chosen as the susceptor material to be investigated in this research, due to cost, availability and high hysteresis heat generation. Three powders were investigated with varying size and shape, shown in Table 2.1. Figure 2.1 shows representative images of the powders. The powder in Fig. 2.1a is the Sigma-Aldrich nanomagnetite (M). The larger apparent particles in the SEM micrograph are actually clusters. Due to humidity and to the magnetic nature of the material, particles have a natural tendency to cluster. This was not realized until after synthesizing the foam samples investigated in the first part of Chapter 3. For the subsequent work in Chapter 3 with solid resin samples, this clustering tendency was mitigated by first submitting the powders to a degaussing routine to demagnetize them, rinsing the particles in acetone and then vacuum drying to eliminate humidity.

Table 2.1: Susceptor particles and supplier specifications

Material	ID	Supplier	Product Number	Form	Particle Size	Density [g·cm^{-3}]
Magnetite (Fe_2O_3)	M	Sigma-Aldrich	637106	Nanomagnetite	<50 nm	4.8-5.1
	N	Sigma-Aldrich	310069	Micromagnetite	<5 μm	
	O	Nanochemonics	B-2540	Acicular nanomag	25 × 400nm	

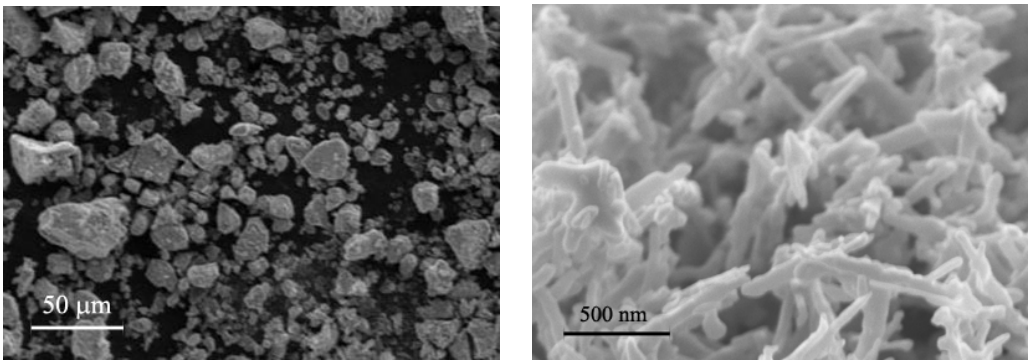

(a) **(b)**

Figure 2.1: SEM images of particle morphology a) spheroidal magnetite particles from Sigma-Aldrich and b) acicular magnetite particles from Nanochemonics.

Processing

The two parts of the resin epoxy were first mixed, and then the powder filler stirred in and sonically agitated to ensure dispersion of particles. The mixture was then poured into a mold. For foam samples, a proprietary chemical foaming step was done at this stage. For either foam or solid, the sample was then cured at room temperature for 24 hours. For solid samples, either a 1 cm diameter mold or a 1mm thick sheet mold was used; for foam samples a 4 cm diameter mold was used. Sample specimens for some tests were cut from the molded shapes using either hot wire or laser.

For foam samples, the initial filler comparisons were made at 5wt% filler content, with subsequent analysis of the Nanomagnetite at 2.5, 5, 7.5, and 10wt% content.

Microstructure Characterization

Computer Tomography

Computer Tomography (CT) scans were used to characterize the bulk microstructure, using a Scanco Medical microCT 40 x-ray microCT scanner at the Georgia Institute of Technology Orthopedic Bioengineering Laboratory at a resolution of 12 μm per voxel edge.

SEM

Digital images from a scanning electron microscope (SEM) were subsequently used to better observe particle morphology and the particle-matrix interface at resolutions down to 2.5 nm/pixel.

Induction Heating

Specific Heat Capacity

To determine specific heat capacity, c_p, a Thermal Analysis Differential Scanning Calorimeter (DSC) Q100 was used, in accordance with ASTM E1269. Samples were massed in aluminum DSC pans with masses ranging from 10 to 20 mg, with a nitrogen purge rate of 10 ml/min. The DSC was heated from room temperature to 150°C, cooled to 0°C, and reheated to 150°C at a rate of 2.5°C/min in order to remove any thermal history of the material. A sapphire standard was then tested using the same method. Specific heat capacity was then determined by

$$C_{p,sample} = C_{p,std} \cdot \frac{\dot{q}_{sample} \cdot m_{std}}{\dot{q}_{std} \cdot m_{sample}} \tag{15}$$

The specific heat for the sapphire standard was known, the masses (m) were measured for both the standard and the sample, and heat flow ($\dot{q}$) was recorded by the DSC for both sample and standard.

Coil Design

Three helical coils made with 6.35mm diameter copper tubing are described in Table 2.2. They were each tested using a foam sample containing 5wt% nanomagnetite at the maximum current of 450Amps. The drive levels of power and frequency were read from the power supply display and the steady state magnetic field estimated using equation,

$$H_D = \frac{N \cdot I}{\sqrt{d^2 + h^2}} \tag{16}$$

based on the coil parameters where N is the number of turns, I is the current, d the coil diameter and h the coil height. This equation is a first order approximation based upon Amperes Law (Eq 6) and neglects frequency effects of sinusoidal electricity. Based on this evaluation, Coil 2 was chosen and test samples designed to fit the coil.

Table 2.2: Coil parameters

	Coil 1	Coil 2	Coil 3
Coil Turns, N	3	4	5
Coil Dia., d [cm]	3.8	1.9	1.9
Coil Height, h [cm]	2.5	3.0	4.2
Frequency, f [kHz]	280	340	330
Max Power, P [W]	392	500	525
Peak Field, H_D [kA·m^{-1}]	29.5	50.9	49.0

Heater Setup

An Ameritherm Hotshot I induction heater with remote heating station was used for specimen heating. The power supply interface allows selection of current level and automatically adjusts power and frequency dependent on selected amperage and coil inductance (which is determined by coil geometry, volume and permeability of the heated specimen). The Hotshot I is capable of power up to 1kW and frequency output of 150-400kHz. The correlation between selected current and automatically adjusted power and frequency for Coil 2 is shown in Fig. 2.2.

Cylindrical samples approximately ∅1×2cm were placed in the center of the coil for testing heating performance. Surface temperature of heated specimens was measured remotely by an Extech IR thermometer located 3-6 cm away.

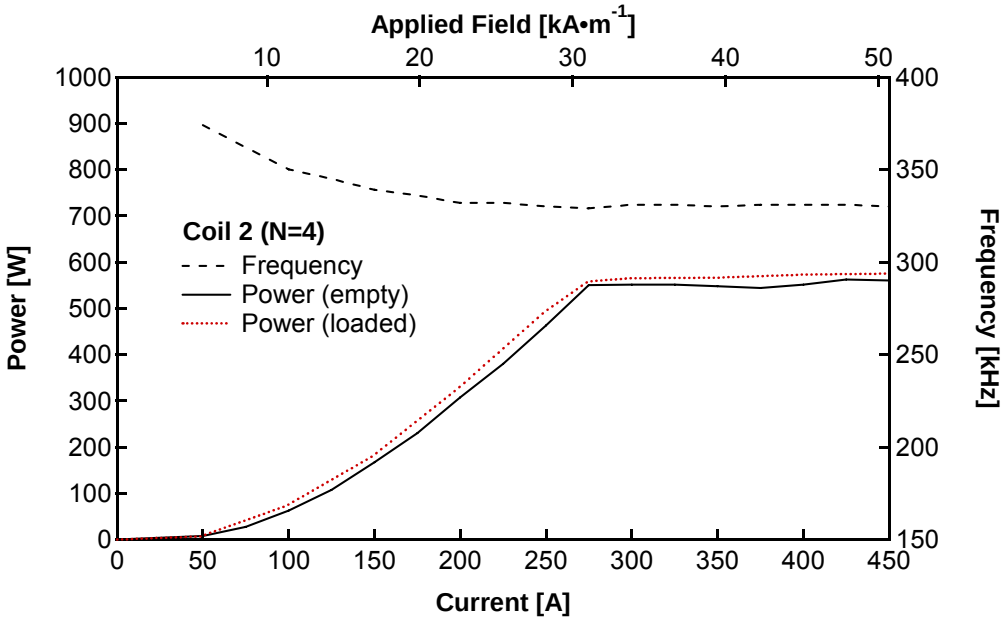

Figure 2.2: Power and frequency calibration curves for Coil 2

Magnetic Properties

Hysteresis

Hysteresis curves were measured using a Lakeshore vibrating sample magnetometer (VSM) with 1cm (nominal) cubic foam samples and 0.8cm (nominal) cubic solid samples. A demagnetization factor of N=1/3 was assumed for calculating the internal field where

$$H_i = H_a - N \cdot M \tag{17}$$

The magnetic moments are measured in *emu* by the VSM and converted to M (in $A \cdot m^{-1}$) based on the volume of the foam samples, which was calculated from the caliper measured sample dimensions.

Thermomechanical Properties

Constrained Stress Recovery

The packaged specimens were placed into the MTS Insight 2 mechanical test frame, with a 100N load cell and attached thermal chamber, and compressed at room temperature to a preload of 0.5N. The compression platen was then raised 0.3 mm to take into account thermal expansion. The platen was then held at that position as the temperature was increased from 25°C to 145°C at a rate of $2°C \cdot min^{-1}$. The stress exerted by the specimen on the platen was then recorded versus time, which was correlated to the temperature.

Free Strain Recovery

A square glass slide, with laser tape along the edge facing the extensometer, was set on top of the packaged specimen. The specimen was then placed on a single compression platen, also with laser tape on the edge (facing the extensometer and parallel to the glass slide), in the MTS Insight 2 with attached thermal chamber. The specimen was then heated from 25°C to 150°C at a rate of $2°C \cdot min^{-1}$, while the MTS LX300 laser extensometer recorded the displacement of the two pieces of laser tape. This displacement was used to determine the percent strain recovered and plotted against the temperature (again correlated with time).

Dynamic Mechanical Analysis

To determine the transition temperature, T_g, a Thermal Analysis DMA Q800 was used with film tension clamps. Samples were cut to dimensions of roughly 1mm×5mm×20mm and inserted in the tension grips. With the use of a torque wrench, the upper clamp was tightened to 0.11 N-m of torque and the lower clamp was tightened to 0.22 N-m of torque. The sample was

equilibrated at 25°C for two minutes and then heated to 150°C at a rate of 5°C·min^{-1}. The test was run under engineering strain control; with a strain of 0.2%, a preload of 0.01 N, a force track rating of 150%, and a frequency of 1 Hz.

Compression and Shape Packaging

Compressive response (and shape packaging) was performed at T_g+10 for the foam composites in a MTS Insight 2 mechanical test frame, with a 100N load cell and attached thermal chamber. To ensure uniform heating, the thermal chamber and each specimen was held at temperature for ten minutes at each temperature. To achieve full contact of the platen on the sample, a preload of 0.075N was used. The cross head speed was set at a rate of 3mm/min for a strain rate of 0.0025s^{-1}. The sample was compressed to 75% of original height and then cooled at a rate of 2°C·min^{-1} until no force was measured by the load cell. Once packaged, the sample was removed from the thermal chamber.

CHAPTER 3: RESULTS AND ANALYSIS

This chapter discusses the results and subsequent analysis of experiments conducted on foam and solid DP5.1 SMP reinforced with magnetite particles. This chapter is organized by first discussing parameters and characterizations common to both foam and solid, then moves into a discussion of the foam experiments, and finally discusses the solid system experiments.

Common Heating Parameters

Specific Heat

In order to calculate heat absorption of the foam via Eq. 17, the specific heat capacity of the samples needed to be known. Specific heat curves are plotted in Fig. 3.1 for foam and solid samples with and without filler. This chart shows that the specific heat for all samples increases fairly linearly up to the transition temperature, then continues to increase at a slightly lower rate thereafter. There is a slight difference in transition temperatures for foam versus solid samples that may be attributed to the chemical foaming process, but the curves for all the foam samples and all of the reinforced solid samples fall within the variation of neat foam values. This suggests that there is no significant microstructure dependence for bulk specific heat (as would be expected for an intrinsic property), as well as hinting at more significant measurement variables that have not been identified yet, responsible for the variation. Subsequently, a standard curve for c_p as a function of temperature is used for all solid and foam samples (regardless of filler content) based upon the average solid foam curve. The standard specific heat book value listed for epoxies[5] of 1.0-1.5 $J \cdot g^{-1} \cdot K^{-1}$ corresponds closely to the values found at 300K in this experiment.

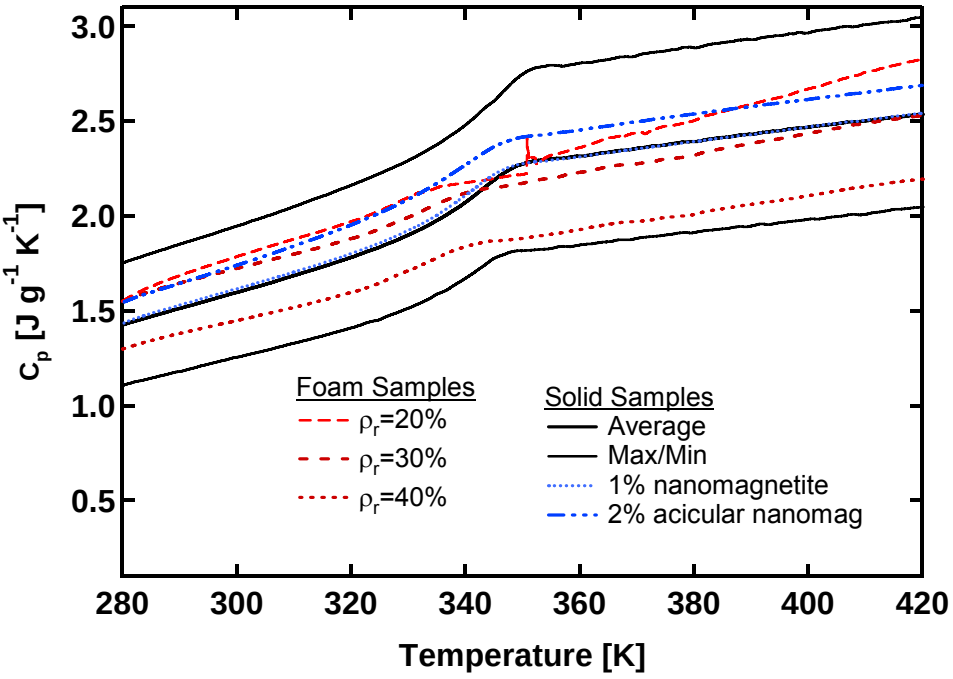

Figure 3.1: Specific heat characterization of DP5.1 solid and foam

Sample Cooling Coefficient Determination

Cooling rates for both foam and solid samples were first measured with the heater off to determine the effective heat transfer coefficients for the samples. Due to the small volume fraction of filler particles, the effect of filler content on cooling was assumed to be negligible. Fig.3.2a shows representative cooling curves of unpackaged solid and foam samples. The data was far too noisy to estimate dT/dt based upon a simple $\Delta T/\Delta t$ of adjacent data points, so cooling rates were calculated using smoothed slopes based on 50-point rolling averages. The heat storage ($\dot{E}_{st}$) term from Eq. 13 was then calculated from the dT/dt curve and the c_p curves (from Fig.3.1) while the loss term ($\dot{E}_{out}$) was simultaneously calculated and compared to determine the heat transfer coefficient due to convection (h) in accordance with equations 11-14. The emissivity was assumed to be 0.97 for all samples. Fig.3.2b shows for both foam and solid samples how

well the calculated heat loss fits the calculated heat absorption when heat generation ($\dot{E}_g$) is zero. Subsequently, for all experiments with foam samples, the heat loss rate was computed based on h=2 W·m^{-2}·K^{-1}; for solid resin samples, h=5 W·m^{-2}·K^{-1}.

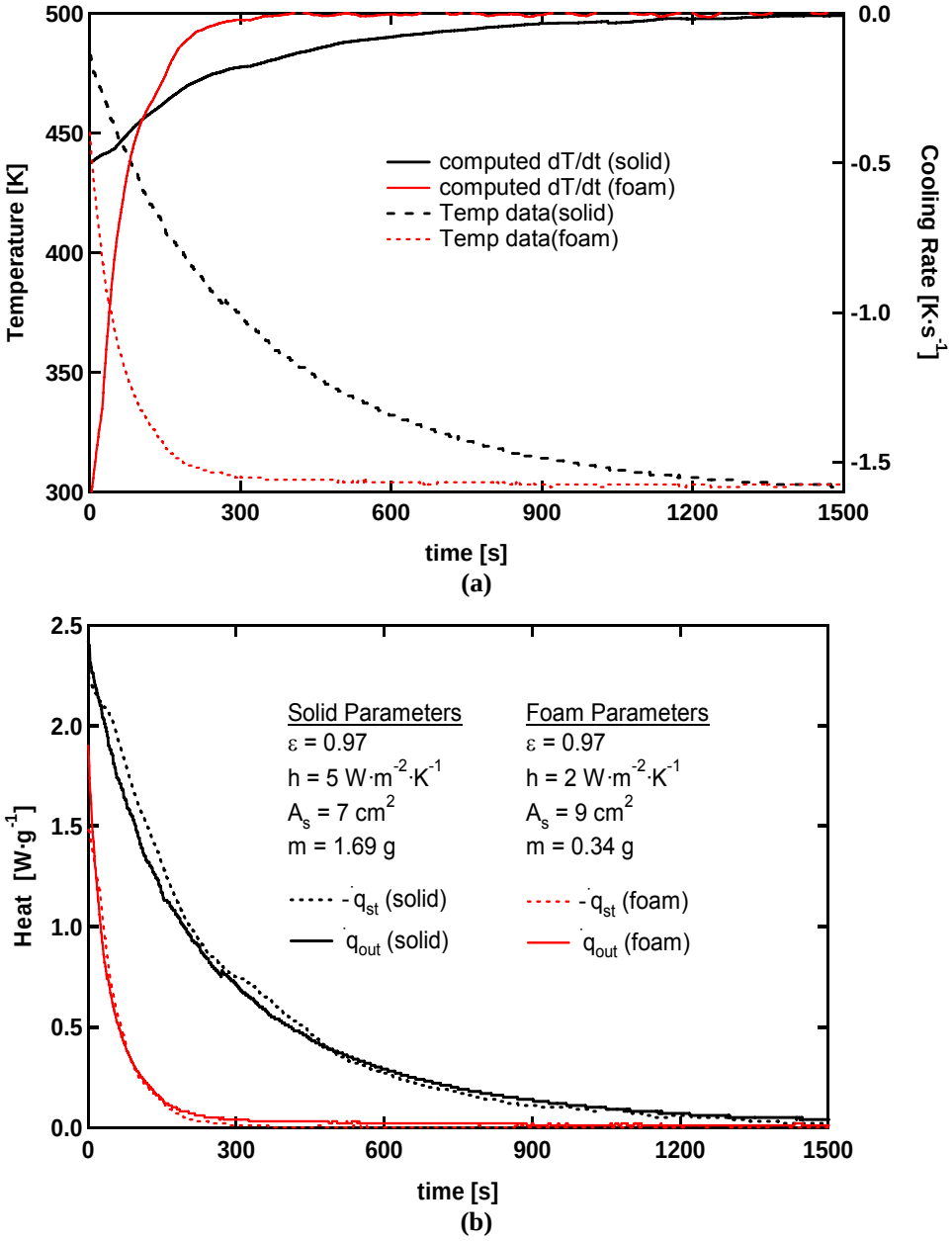

Figure 3.2: Sample cooling for solid and foam samples without reinforcement. a) cooling rate curves computed from a rolling average slope of the cooling data curves, and b) heat storage versus heat dissipation.

SMP Foam Analysis

Despite being the more complex system, foam samples were investigated at the chronological outset of this research in order to provide proof of concept and validate the overall approach of the project. The foam samples were prepared by CTD using nanomagnetite powder.

Microstructural Characterization

The DP5.1 foam investigated is primarily an open cell structure with a small percentage (<10% by volume) of closed cells. The relative density of the samples used was in the range of 15-20% in the as-fabricated state (or initial unpackaged state). Although the hysteresis heating of particles is dependent upon the total particle volume, the variability in relative density of the foam structure as well as packaging conditions makes it inherently difficult to compare volume fractions on a relative basis. As such, foam samples were processed and compared by wt% of particulate filler, rather than by volume fraction. Table 3.1 shows the variation in relative density for the samples used and correlates the nominal weight percentage to unpackaged (0% compression) volume fraction.

Table 3.1: Physical data for foam samples with nanomagnetite reinforcement

	NF	NM2.5	NM5	NM7.5	NM10
Particle Wt %	0.0	2.5	5.0	7.5	10.0
Sample Density, ρ (g/cm^3)	0.174-0.218	0.207	0.164	0.218	0.196
Volume fraction of resin, v_r	0.160-0.200	0.185	0.143	0.185	0.162
Volume fraction of particles, v_p	0.0	0.0010	0.0016	0.0032	0.0038
Volume ratio, V_p/V_r	0.0	0.005	0.011	0.017	0.024

Fig. 3.3 shows micro computer tomography (CT) scans of foam samples containing 2.5-10 wt% nanomagnetite filler, showing long-range homogeneity in particle dispersion. What appears to be relatively larger particles or particle clusters is due to partially to CT resolution

(12μm/voxel), and partially due to shadowing of the denser particles. This makes it meaningless to perform a quantitative stereological analysis of particle content or size distribution.

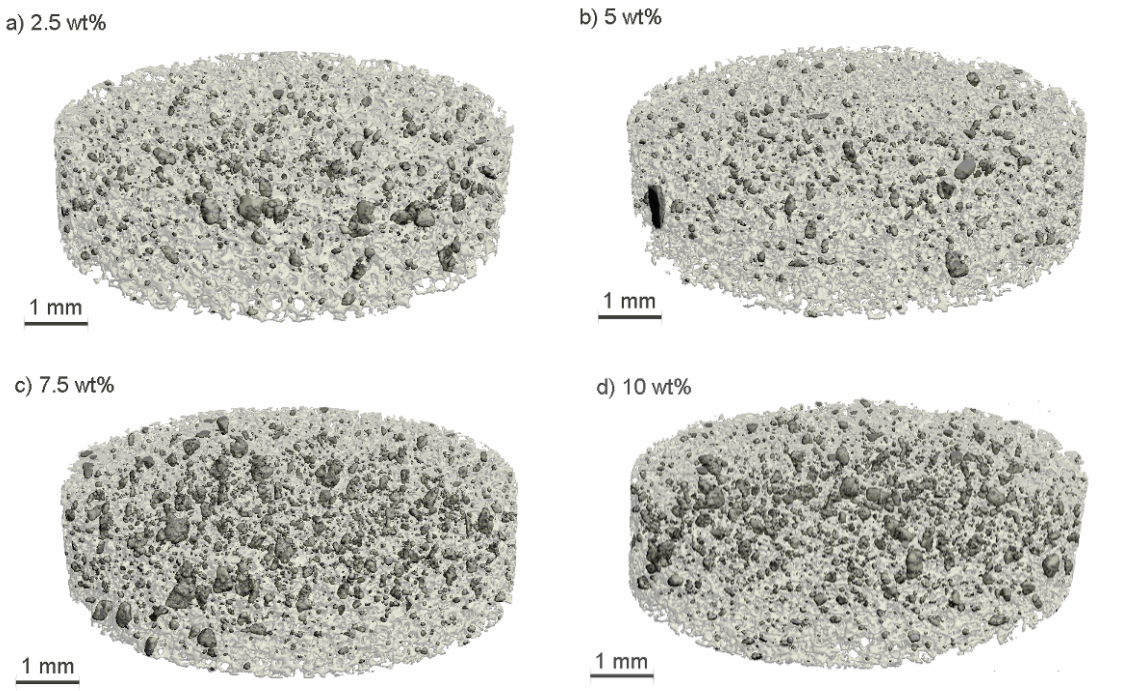

Figure 3.3: CT characterization of DP5.1 foam samples with a) 2.5wt%, b) 5wt%, c) 7.5wt%, d) 10wt% nanomagnetite particles

Fig. 3.4 shows a representative foam structure of a sample with 5wt% nanomagnetite particles embedded in the resin matrix. These images confirm that some of the particles were up to 20 μm diameter, contrary to supplier specifications.

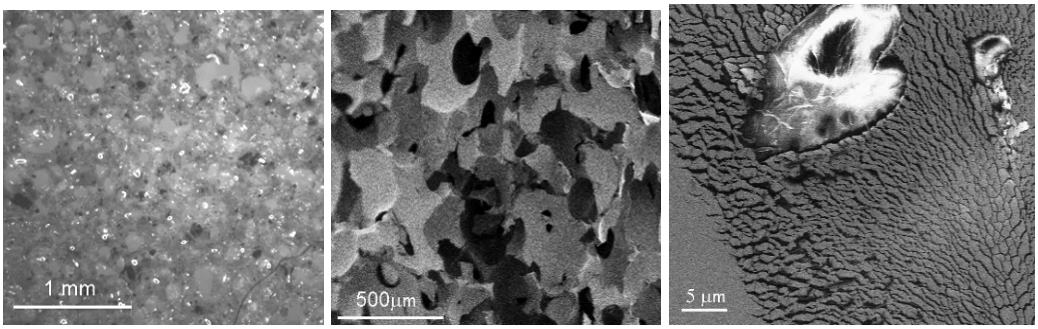

Figure 3.4: Images of SMP foam composite with 5wt% nanomagnetite filler showing cellular foam microstructure, via a) optical microscopy, and b) SEM view of strut microstructure, as well as c) SEM showing particles embedded in polymer matrix.

Heating Performance

Cylindrical foam samples were placed in the center of induction coils at room temperature, and heated using electromagnetic induction. Surface temperature was recorded throughout the heating process. Imagery from a FLIR infrared camera visually shows in Fig. 3.5 the heating process with localized hot spots immediately upon applying the alternating field (3.5b) and at the transition temperature (3.5c). The hot spot pattern is consistent with the type of particle distributions revealed in the CT scans, and indicates that hysteresis is the primary heating mechanism, since eddy current heating characteristically manifests as a skin effect in the bulk sample. Once the field is removed, the cooling process shows a much more homogenous temperature gradient (3.5d).

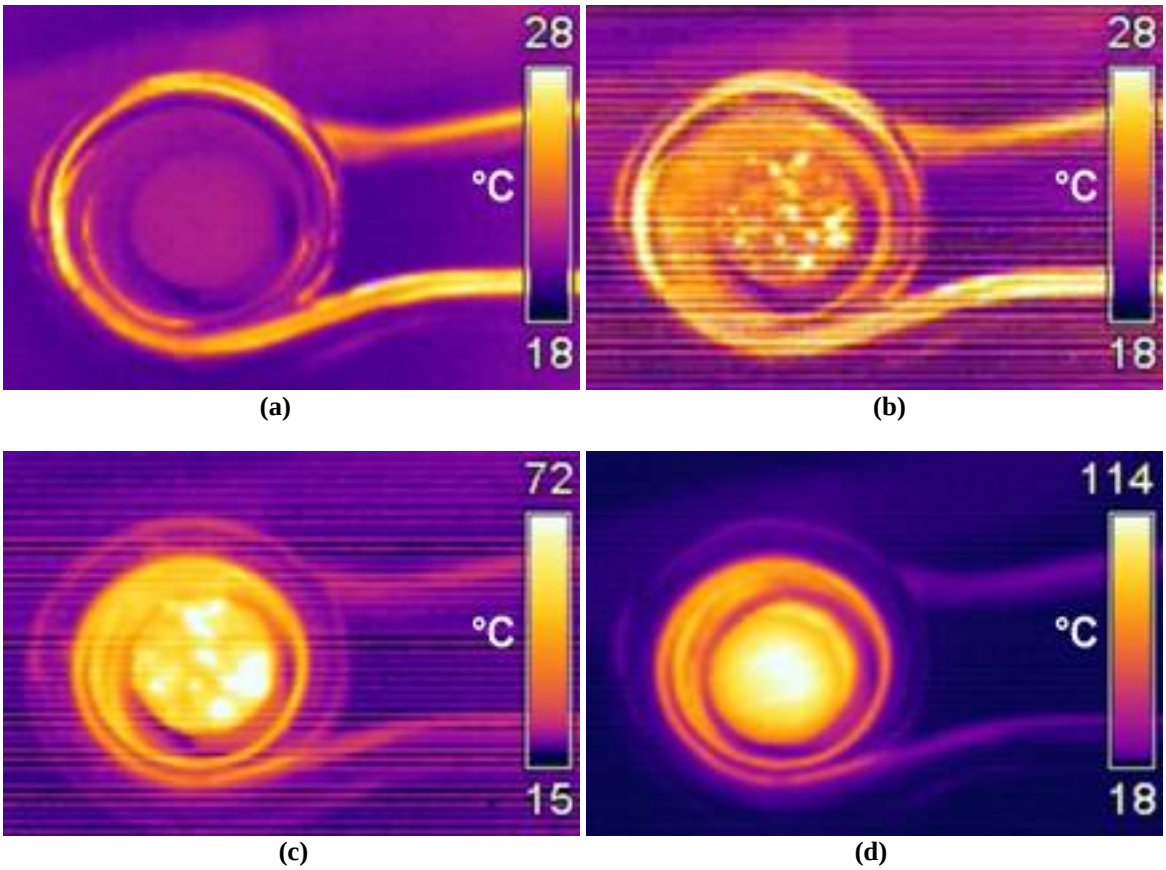

Figure 3.5: Coil 2 heating of DP5.1 foam with 10wt% nanomagnetite, a) just prior to starting induction heater, b) immediately after turning on, c) at transition temperature, and d) during cooling (after heater has been turned off). The lines in b-c are due to EMI from the coil.

The influence of nanomagnetite filler fraction on heating was investigated for weight percentages between 2.5 and 10wt%. Fig. 3.6 shows the heating performance comparison of foam samples containing varying amounts of the nanomagnetite filler, using Coil 2 with 450A current. Although these curves are not normalized for sample size, the figure shows a general increase in heating rate (given by the slope of each heating curve) for increased filler content. For each sample, data from five sequential heating cycles is shown in order to indicate the magnitude of variation in runs and to investigate any short term thermal degradation in heating performance. Although there was no indication of thermal fatigue trends affecting the heating performance over the small number of cycles tested, there was significant variation in heating performance between runs, especially for the 2.5wt% sample. Sources of variation between heating runs may have been due to sample placement within the coil, and to placement of the IR thermometer spot on the sample. This is a subject for future investigations, since practical application necessitates a high degree of predictability.

For each curve, a best linear fit was determined based upon the average heating over the first minute. Other fit models are a subject for exploration later in this chapter, but the simple linear fit has the advantage of providing a single value approximation for heating rate (dT/dt).

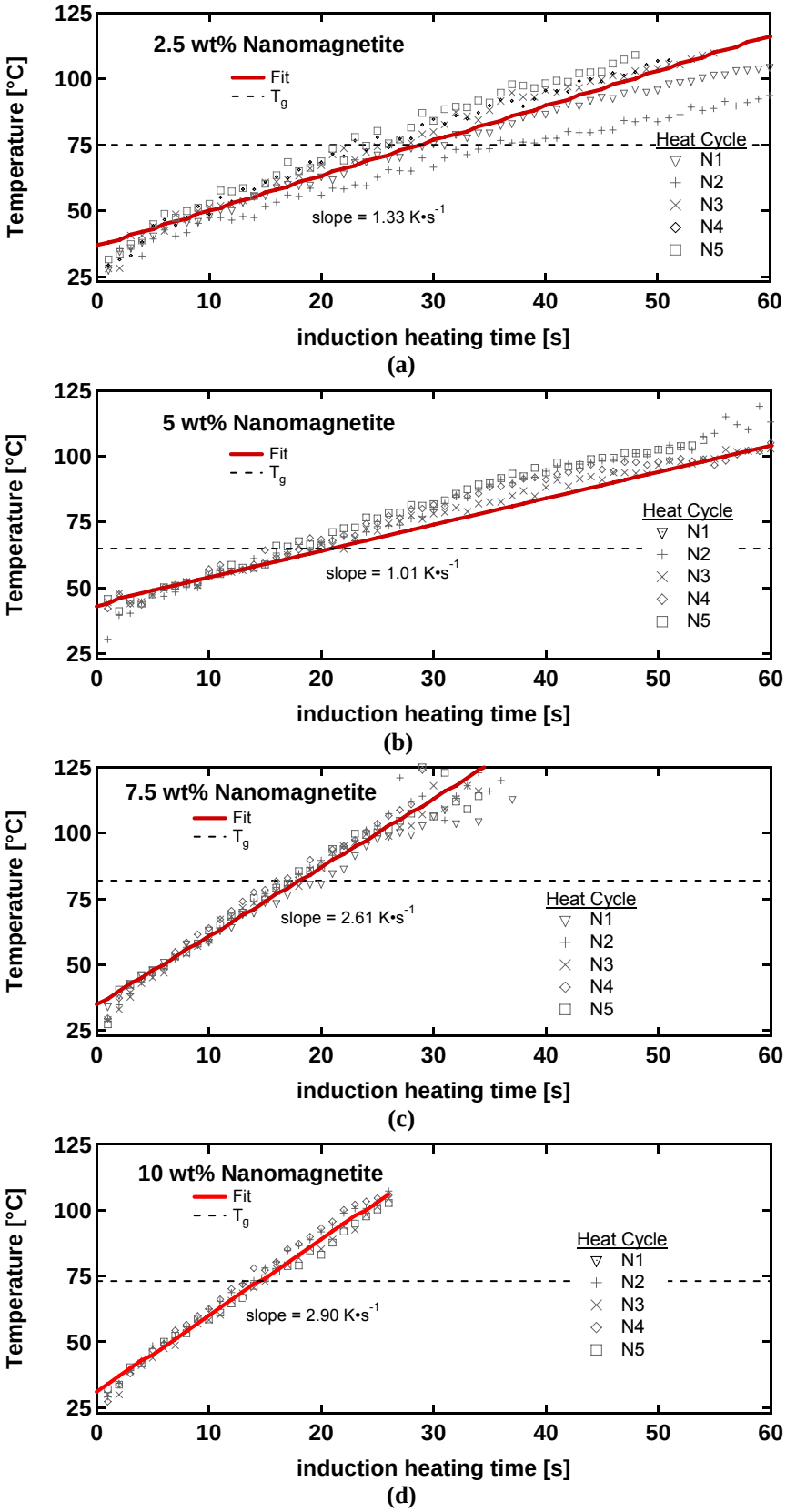

Figure 3.6: Induction heating curves of DP5.1 foam with a) 2.5 wt%, b) 5 wt%, c) 7.5 wt% and d) 10wt% nanomagnetite. Multiple heat cycles were recorded for each sample and best line fit to the first minute.

The estimation of dT/dt enables quick calculation of the specific thermal power ($P_a = \dot{E}_{st} / m$) absorbed into the foam as given by Eq. 18 where *m* is sample mass. A specific heat of 1.5±0.5 $J \cdot g^{-1} \cdot K^{-1}$ is used to calculate the specific power absorption values shown in Fig. 3.7. Although there is some discrepancy between 2.5 and 5 wt%, there is otherwise a general increase in power absorption for increased filler content. The relation follows a linear relationship with an absorption coefficient, κ, equal to the slope in Fig.3.7, relating filler content with the specific power absorption. For this coil and these power settings, $\kappa = 0.455\ W \cdot g^{-1}$.

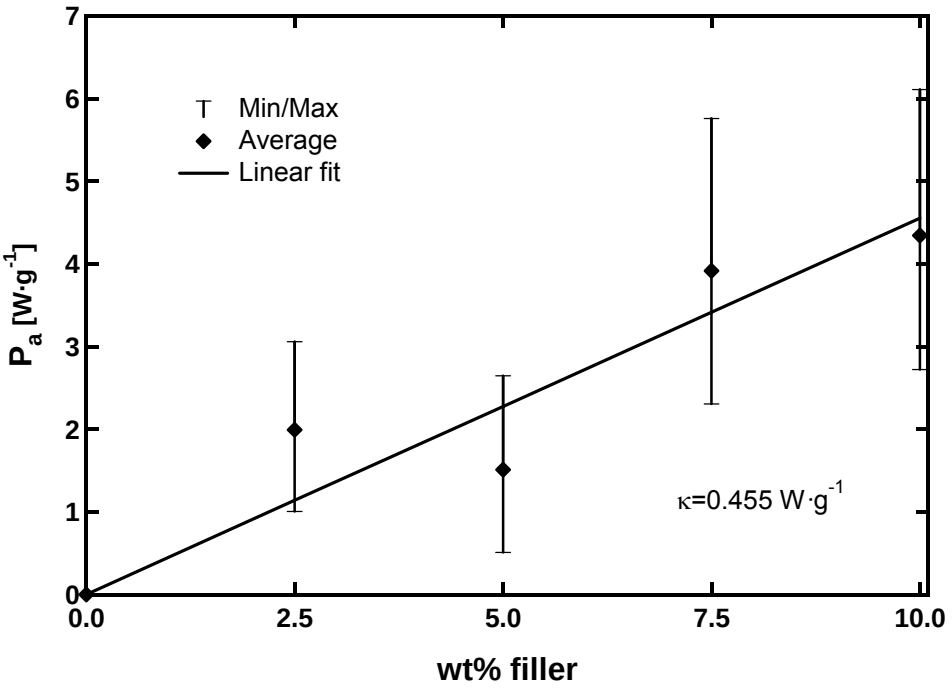

Figure 3.7: Specific power absorption of induction heated DP5.1 foam samples with nanomagnetite filler. The shaded band shows the maximum and minimum calculated absorption values based on error analysis.

Magnetic Properties

The hysteresis heating power is determined by the shape and magnitude of the hysteresis curve. A vibrating sample magnetometer (VSM) was used to characterize the magnetic response for the nanomagnetite filler samples. Typical curves are shown in Fig. 3.8 for the four samples.

Table 5 lists the key parameters for the samples representing the four loading levels, with the specific heating power calculated in the bottom row for a frequency of 330 kHz. As shown in previous studies with nanoparticles, the saturation scales with the volumetric particulate content[19]. Although the VSM characterization was done at near static conditions (~0 Hz), subsequent impedance analysis indicated no significant frequency dependence under 1 MHz.

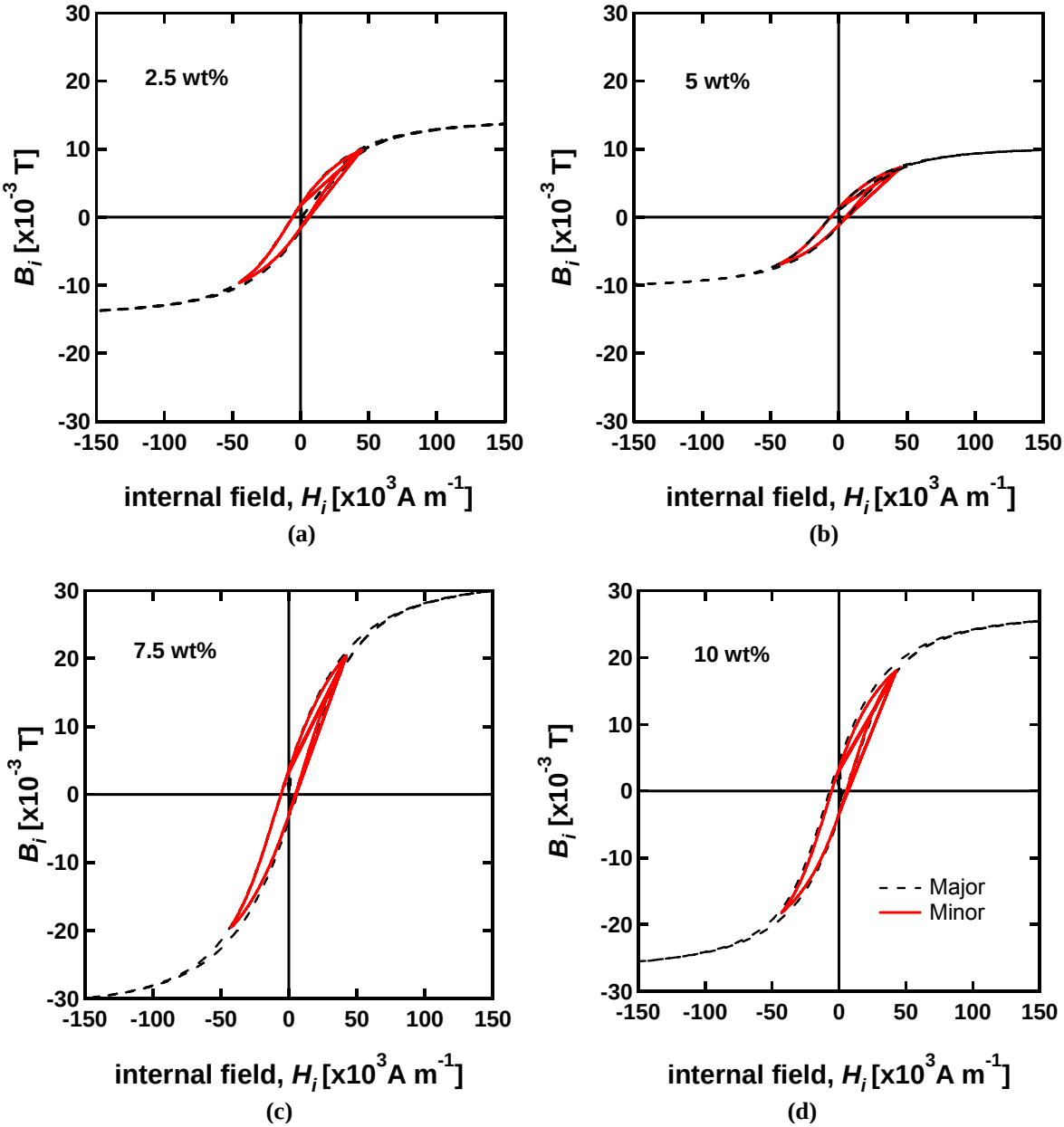

Figure 3.8: Magnetic hysteresis curves for DP5.1 foam with nanomagnetite filler. a) 2.5 wt%, b) 5 wt%, c) 7.5 wt%, and d) 10 wt% nanomagnetite

Table 3.2: Bulk magnetic properties comparison of DP5.1 foam with varying amounts of nanomagnetite filler particles

	2.5 wt%	**5 wt%**	**7.5 wt%**	**10 wt%**
Sample Dimensions, $L \times W \times H$ [cm]	1.1x1.0x0.9	1.2x1.0x1.0	1.0x0.9x0.9	1.3x1.1x0.9
Sample Density, ρ [g·cm^{-3}]	0.17	0.19	0.22	0.14
Remanence, B_r [mT]	2.2	1.2	3.1	5.4
Saturation, B_s [mT]	1.9	1.6	4.1	3.7
Coercivity, H_c [kA·m^{-1}]	5.52	4.80	5.28	5.55
Minor loop work, W_h [mJ·cm^{-3}]	0.16	0.20	0.30	0.29
Specific Power @330kHz, P/m [W·g^{-1}]	310	362	450	700

Taken together with the CT scans and heating curves, it is probable that the filler content is not exact and that the 2.5 wt% (nominal) sample actually contains as much, if not more filler than the 5wt% (nominal) sample. It is likewise probable that the 7.5wt% (nominal) and 10wt% (nominal) samples have a comparable amount of filler.

Mechanical Properties

Storage modulus and tan delta as a function of temperature are shown in Figure 3.9 for pure foam and the four nanomagnetite reinforced samples. Neither the modulus nor T_g seems to be affected by relative density of the material or by nanomagnetite content. Previous work on

reinforcing SMPs with magnetite has shown no effect on T_g, for increasing content, but relative density should show a corresponding increase in modulus[20, 23].

Fig. 3.10 demonstrates that the filler content has little effect on the compressive response of the foams in light of the significant effect of foam relative density. The importance of relative density on the compressive response is expected[23]. At the highest loading of nanomagnetite (10wt%), the volume fraction of particles in the polymer is less than 2.5% and it is therefore reasonable that foam microstructure dominates the deformation response.

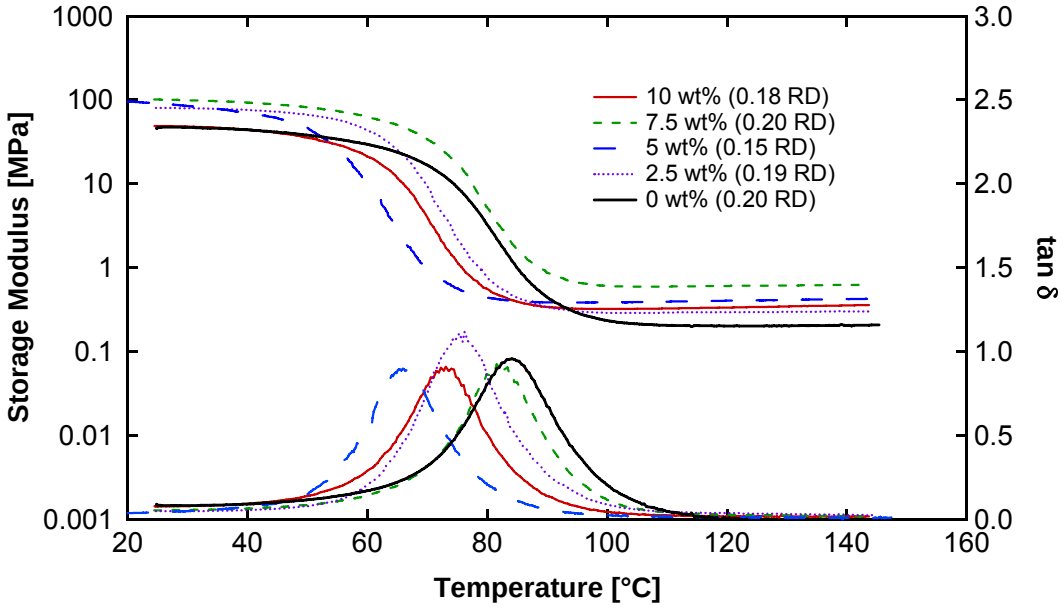

Figure 3.9: Dynamic mechanical analysis of DP5.1 foam with nanomagnetite filler

Figure 3.10: Compression of DP5.1 Foam with Nanomagnetite Filler (at T_g)

Fig. 3.11 quantifies the externally controlled temperature shape recovery responses as a function of temperature for the five foams. In Fig. 3.11a, constrained recovery stress shows no trend in terms of reinforcement concentration but a strong trend in terms of relative density. In

Fig. 3.11b free strain recovery shows that the particle reinforcement has an insignificant effect on externally thermally activated shape recovery. The jogs in the curves are the result of non-uniform recovery in the sample, likely due to local non-uniformity in cell size. At least for the range of particle content investigated, processing and relative density are the dominating factors in mechanical properties enabling volume fraction of particles to be chosen within the range studied here to optimize heating response without significantly influencing the thermo-mechanical properties of the base resin. On the other hand, the volume fraction of particles is expected to influence remotely activated shape recovery response due to differences in induced heating rate and magnitude.

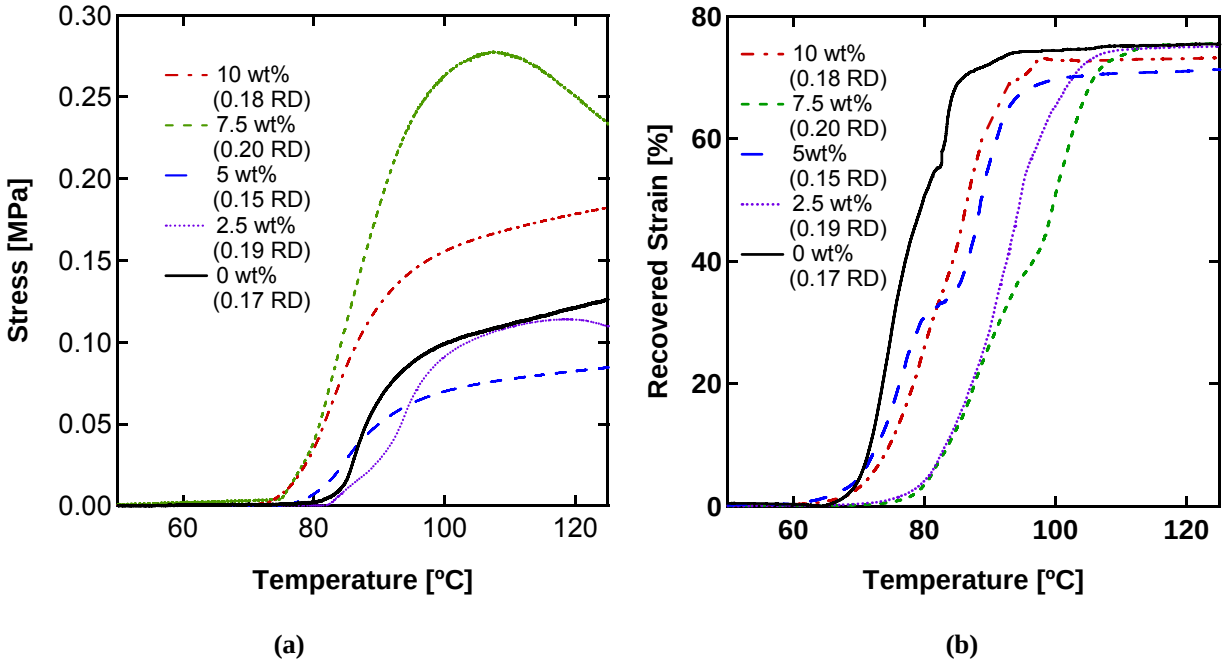

Figure 3.11: a) Constrained and b) Free Recovery of DP5.1 Foam with Nanomagnetite Filler

Remote Activation Performance

The ultimate purpose of heating SMPs is to activate recovery, so foam samples with 75% packaged strain were investigated. Fig. 3.12 shows the recovery of this sample superimposed

with the heating curve (similar to the ones in Fig. 6 or 7a) for both 5wt% and 10wt% Nanomagnetite reinforcement. As previously demonstrated and discussed, the 2.5 and 7.5wt% sample performed similar to the 5 and 10wt%, respectively. The transition temperatures are indicated by the dashed lines at 65 and 73°C, respectively. Even though the 5wt% sample had the lower transition temperature, the fastest recovery occurred in the 10wt% Nanomagnetite filled sample with recovery beginning at around 10 seconds and completing after an additional 7 seconds. Recovery rate in both samples increases rapidly when the temperature of the sample crosses the T_g of the material, highlighted by the crossing of the dashed lines in Figure 3.12. The recovery times are consistent with the induction heating times demonstrated and reported by other investigators. Recovery occurs unevenly over the course of heating. The recovery is also spatially uneven, with typically one side of the sample recovering a second or two faster than the other side. This phenomenon may be due partially to uneven heating (caused by off-center positioning in the coil, hotspots from large particles/clusters, or large voids in the resin); however, as previously noted, similar non-uniform recovery behavior observed during external heating of samples in the free recovery trials suggests that this phenomenon is inherent to the recovery of foam SMP structures at this scale.

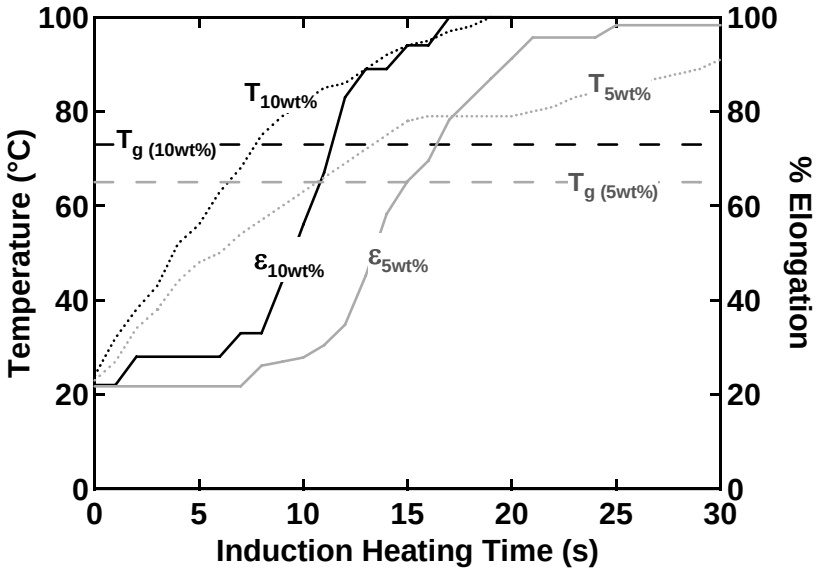

Figure 3.12: Recovery of 75% packaged DP5.1 foam samples with 5 wt% and 10wt% nanomagnetite filler, using Coil 2.

An overview of the heating efficiency of the induction method is shown in Fig. 3.13. All of the samples showed the potential to absorb 50-80% of the applied power in the form of hysteresis loss in the filler particles. However, the heat flow rate appears to be limited between the particles and the resin, with less than 1% of the initial heat measured as heat absorption at the sample surface. This indicates that the greatest opportunity for increasing the heating performance (i.e. decreasing time to reach T_g) lies in improving the heat transfer between particles and resin, as well as within the bulk foam itself. Initially it was assumed that the particles would be dispersed well enough that heating of the foam would not be strongly dependent on foam microstructure. However, as the IR imagery clearly demonstrates, heating *is* non-uniform on the macroscopic scale, so cell structure probably does impact the heat flow away from the hot spots.

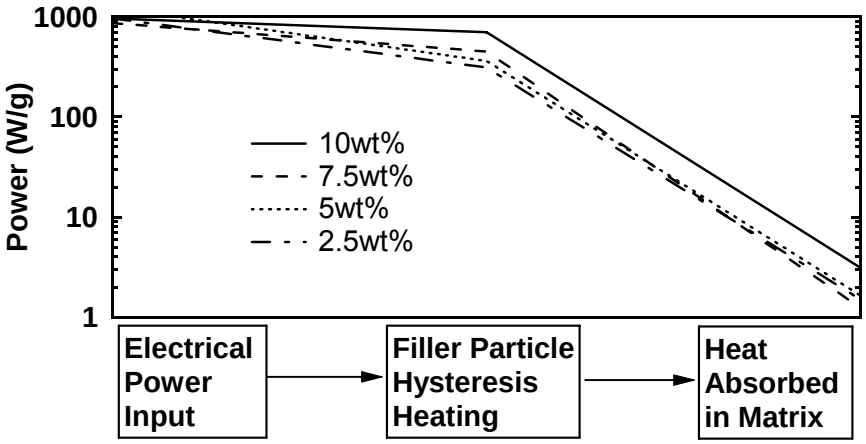

Figure 3.13: Heat absorption of DP5.1 foam samples with nanomagnetite filler

Composite Design Parameters

A deeper understanding of the material design parameters warranted further investigation into the simpler solid resin composite system exploring additional particle and processing variants, as well as further exploration of analysis techniques for heating. The previous section showed that the best opportunity for faster heating was in improving the heat transfer in the matrix and from the susceptor particles to the matrix. The simplest design parameter to change for affecting heat transfer is the surface area of the interface (as highlighted in Eq, 10). This surface area is primarily controlled by the number, size, and shape of particles. For a given volume of particles the number and size are inversely proportional. As shown in Fig.3.14, the volumetric surface area is a function of the size and shape. Fig.3.14a shows an exponential increase in surface area as particle size is decreased. The BET method is the most common way to measure this and the supplier specifications for the powders listed in Table 2.1 are charted in this figure as well, showing the equivalent surface area based on the nominal density of magnetite ($\rho = 5$ g·cm^{-1}). Fig. 3.14b shows the effect of aspect ratio on the surface area for particles of equivalent volume, for two different characteristic sizes.

Particle size and shape also affect magnetic properties. Further discussion of this can be found in Appendix A.

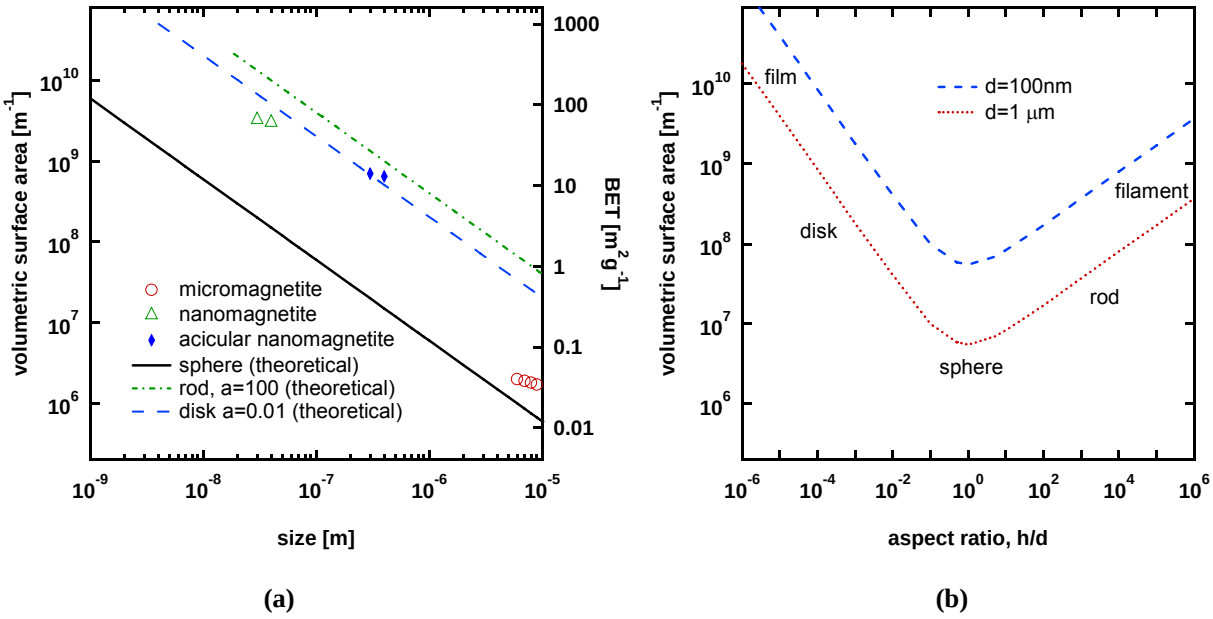

Figure 3.14: Particle surface area as a function of size and shape. a) characteristic size of theoretical shapes are shown as lines; powder used are shown as markers, b) surface area dependence on shape for two different particle sizes.

For the solid resin experiments, filler content comparisons were made based upon volume percent rather than weight percent. The relation to the filler loading in the foam experiments can be seen through the V_p/V_r ratios listed in Table 3.1.

Heat Curve Fitting

Computing dT/dt based on noisy data provides irregular results, so the key to analyzing power absorption lies in finding a fit model that can be easily differentiated. As shown by other researchers, the heating curves are expected to be semi-sigmoidal, approaching a steady state temperature that is determined by the convection/radiation cooling rate. Our experiments were all carried out to a maximum of 200 seconds, or 200°C, whichever was achieved first. Additionally, if samples began to smoke, the induction heater was turned off, so as to minimize

any thermal damage to the samples. These limits prevented the achievement of thermal equilibrium in any of our experiments. Furthermore, most practical applications require SMP activation (i.e., achieving T_g) in less than 30s.

This section examines four alternative fitting models: linear, cubic polynomial, power, and Ramberg-Osgood. Fig. 3.15 shows the heating curve for a solid resin sample containing 0.5vol% nanomagnetite filler. The experimental points shown are the average of three runs in coil 2 at 300A ($H \approx 34$ kA·m^{-1}). The four fit models are plotted in the top graph and the residuals (fit temperatures minus experimental temperatures) are plotted in the bottom. All four models were fit using the least squares method. ΔT is the temperature change from the initial temperature (T_o=T(t=0)). The residual is the difference between the measurement average and the fit temperatures.

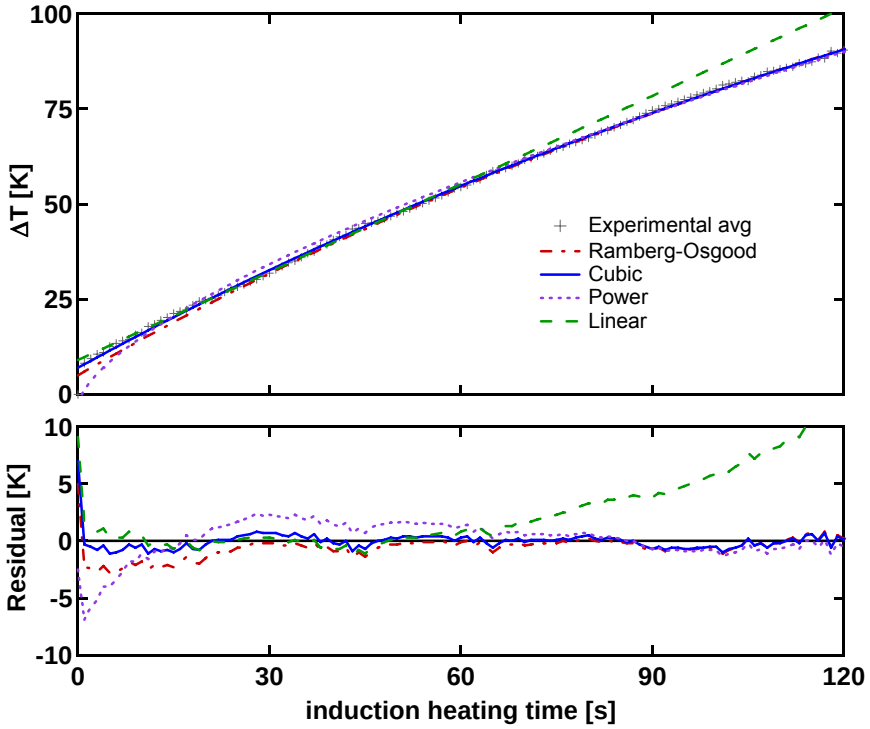

Figure 3.15: Comparison of fit methods. Heating curve data shown is average of 3 runs in coil 2 at 300A using DP5.1 solid resin with 0.5vol% nanomagnetite filler. Four fit methods are shown with residuals plotted in lower graph.

Linear

The linear model (Eq. 18) is the simplest to fit to data and has the advantage of providing a single slope value (dT/dt=*m*) for comparison.

$$T_{fit}(t) = m \cdot t + b \tag{18}$$

However, as shown in Fig.3.15, the single slope does not account for the observed fact that the slope is a function of time. This is most apparent at time t=0 and as heating time approaches infinity. However, it can be assumed that the initial temperature readings are significantly weighted by the hot filler particles. Since the resin matrix (in which we are interested for the purpose of activation) should lag the bulk surface measurements in heating, this initial poor fit is acceptable for most estimation purposes. Line fitting was subsequently based on the first 60 seconds of heating, excluding the intial (t=0, 1, 2) data points.

Cubic

The cubic fit (Eq. 19) is also simple and, within the fitting range, it best captures the time dependence. Like the other fit methods evaluated, it is purely empirical. The cubic model can be expected to diverge significantly over time, since T_{cubic} approaches infinity rather than a steady state constant as time approaches infinity.

$$T_{fit}(t) = a \cdot t^3 + b \cdot t^2 + c \cdot t \ + d \tag{19}$$

Power

The power fit (Eq 20) approaches a constant heating rate, and has a quick take off, to emulate the measured high initial temperature increase.

$$T_{fit} = A + B \cdot t^{N} \tag{20}$$

There is not a unique solution using this method, unless N is constrained. For fitting our data, N was arbitrarily set to 2/3.

Ramberg-Osgood

The Ramberg-Osgood equation (Eq. 21) was originally developed as a description of stress-strain relations. Suwanwatana, et al (2006) used this empirical method for fitting heat curves. Unconstrained, it also does not provide a unique solution for all parameters, but most of the parameters can be defined based upon experimental conditions such as the ambient air temperature (T_a), the initial heat rate ($dT/dt|_o$) and the steady state temperature (T_∞).

$$T_{fit}(t) = T_a + \frac{t\left.\frac{dT}{dt}\right|_{t=0}}{\left(1 + \left(\frac{t\left.\frac{dT}{dt}\right|_{t=0}}{T_\infty - T_a}\right)^{N}\right)^{1/N}} \tag{21}$$

However, since our data did not provide a steady state temperature, this model was cumbersome to use for fitting and the only free parameter, *N*, does not contribute toward any meaningful analysis.

Until a physical model based on heat transfer mechanisms is developed, the linear model appears to be the most useful for further analysis.

Field Strength

Induction heater current was varied in order to understand the relation between the applied field and the heating rate. Fig. 3.16 shows the resulting heating curves for a solid resin sample with 1 vol% nanomagnetite filler. It can be seen that increased field generally increases the heating rate, but above 250A ($H_d \approx 28.2$ kA·m^{-1}) the rate approaches a maximum.

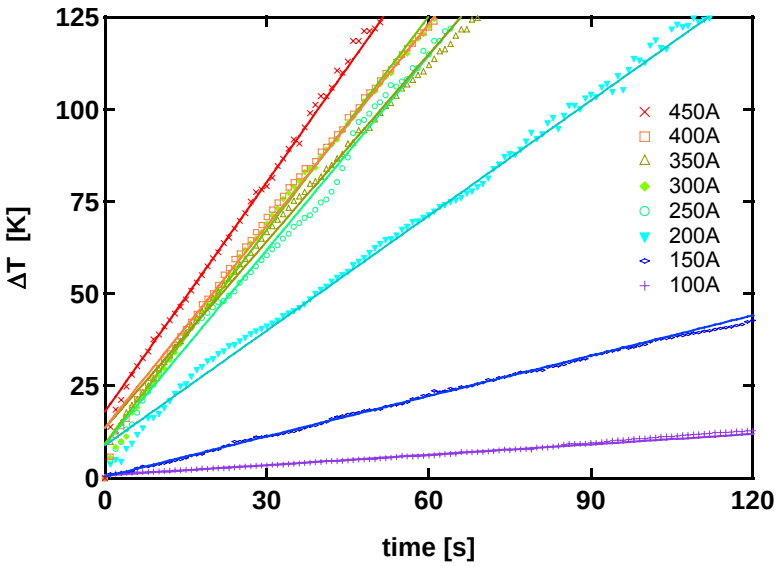

Figure 3.16: Heating curves for solid DP5.1 resin with 1vol% nanomagnetite filler. Heating curve data shown is average of 3 runs in coil 2 at various current levels. Line fits are based upon data between 3 and 60 seconds.

Filler Content

Fig. 3.17 summarizes all of these heat curves, plotting the linear heating rates as a function of current for samples containing varying amounts of nanomagnetite. The dashed lines indicate the minimum and maximum slopes from three runs, with the markers indicating the average. This chart shows a general increase in heating for increased filler content, just as was previously seen in the foam experiments.

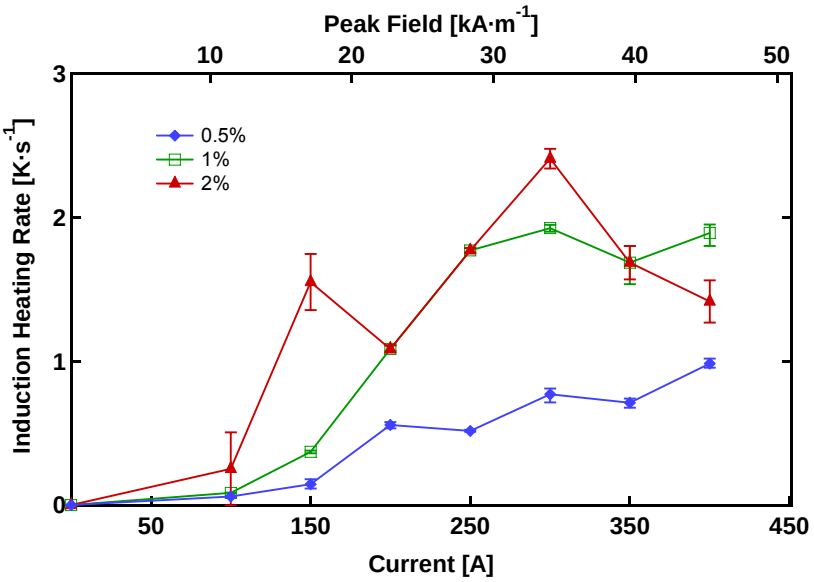

Figure 3.17: Effect of filler content and field amplitude on hysteresis heating rate. Heating rates are calculated from linear fit of heating curves for samples containing 0.5, 1, and 2vol% nanomagnetite filler. Coil 2 was used with the estimated peak field shown on the top axis, and current setting on bottom.

Particle Size and Shape

To evaluate the effect of particle size and shape, samples were made containing 1 vol% of micromagnetite, nanomagnetite or acicular nanomagnetite powders. The acicular nanomagnetite powder was either randomly oriented or aligned in the axial direction (long dimension || applied field) by applying a static magnetic field of 0.5T for the first 1 minute of curing. The scale of alignment is shown in Fig. 3.18. Although individual particles are not visible in this micrograph, the overall alignment into a filamental microstructure can be observed.

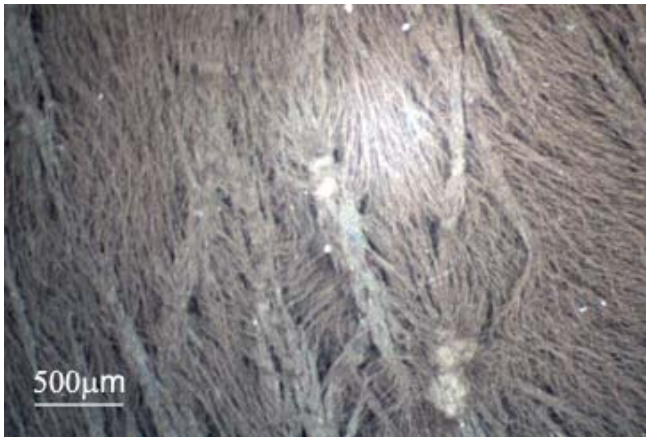

Figure 3.18: Optical microscope image of 2vol% aligned acicular nanomgnetite embedded in DP5.1 resin.

Heating

Fig. 3.19 shows the relative performance of the various susceptor particles. The data shows that there is little difference in performance between the micromagnetite and the nanomagnetite powders. The aligned acicular nanomagnetite also performs comparably at high field levels, while the randomly aligned acicular nanomagnetite performs significantly poorer, within this range of field strength. This behavior suggests a higher coercivity, contrary to expectations for the smaller acicular powders. There are at least two possible explanations for the asymptotic approach to a maximum heating rate:

1) Higher amplitudes of current put the peak applied field into the saturation region of the hysteresis curve, so further increases add very little hysteresis energy.

2) Another scenario is that the heat rate is limited by the geometric and thermal properties of the interface.

Which of these explanations is more valid may be determined by evaluating the hysteresis curves for these materials.

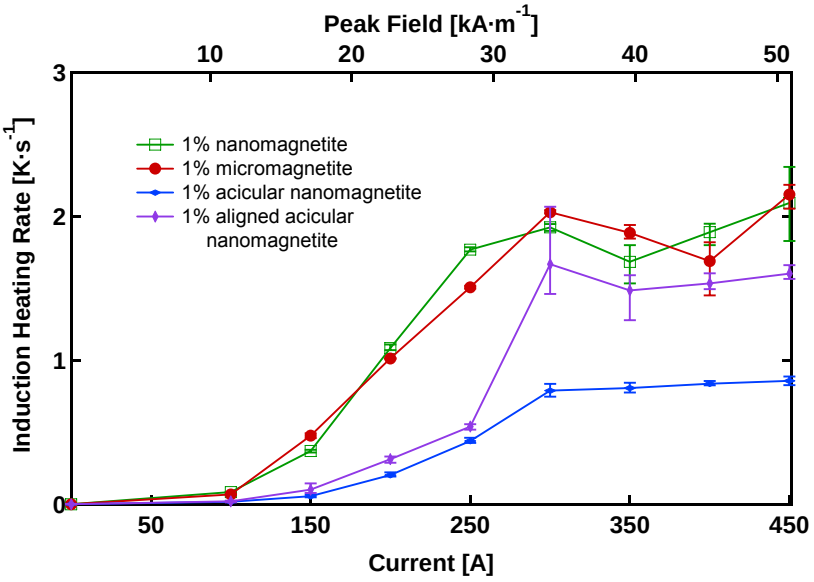

Figure 3.19: Effect of filler type and field amplitude on hysteresis heating rate. Heating rates are calculated from linear fit of heating curves for samples containing 1vol% filler. Coil 2 was used with the estimated peak field shown on the top axis, and current setting on bottom.

Hysteresis Verification

VSM measurements were conducted on solid resin samples with 1vol% acicular particles. Comparison measurements were also done with 1vol% nanomagnetite samples. Hysteresis loops for two minor loops (H_d = 24 kA·m^{-1} and H_d = 40 kA·m^{-1}) were done along with a major loop (H_d = 200 kA·m^{-1}). Measurements were taken in the axial and transverse directions. The resulting hysteresis curves are shown in Fig.3.20. As expected, the hysteresis loops for the acicular particles are much larger at higher drive levels, but not necessarily so at lower drive levels. Although the unaligned acicular sample gave a larger overall area, the saturation (loop height) is very sensitive to filler concentration, as suggested by Suwanwatana[18], so for powder comparison purposes it is better to just compare coercivity (loop widths). The dependence of loop width on drive level is shown in Fig.3.20 for each of the powders. As previously noted in Table 2.2 and shown in Fig.2.2, the peak field generated by Coil 2 at 450A is 51 kA·m^{-1}. At 300A, Coil 2 generates a field about 34 kA·m^{-1}. This is about where the take-off point is for the

acicular particles in Fig. 3.19. Fig. 3.21 confirms that the regular nanomagnetite has a slightly lower takeoff than the acicular. These results highlight the sensitivity of hysteresis loop height (and the subsequent heating rate) to the susceptor content.

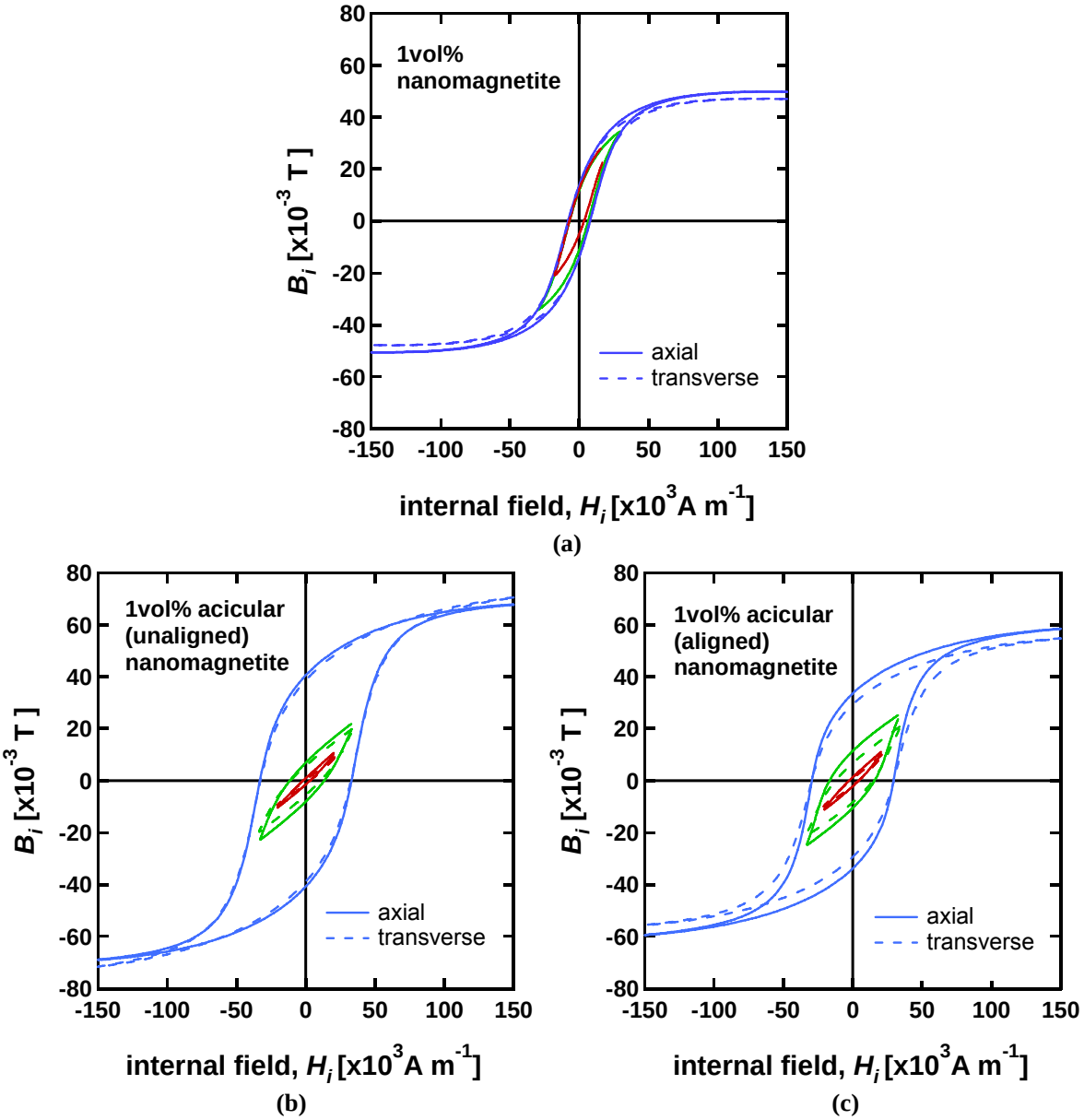

Figure 3.20: Hysteresis comparison of nanomagnetite powders. a) 1% nanomagnetite, b) 1% acicular nanomagnetite, and c) acicular aligned nanomagnetite. Three drive levels are shown, from the center of each graph, outward: 24 kA/m, 40 kA/m, and 200 kA/m.

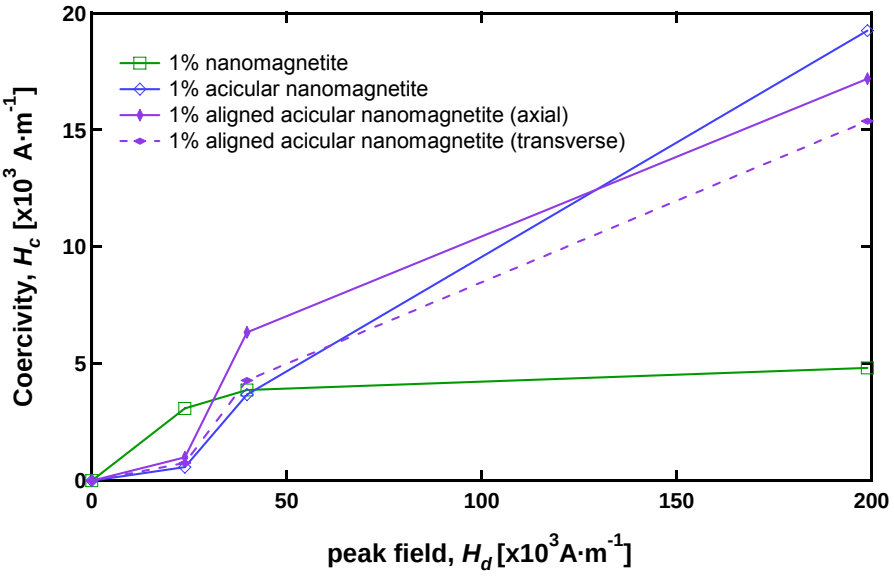

Figure 3.21: Coercivity comparison of nanomagnetite powders.

These results also indicate that the probable mechanism responsible for limiting heat rate during induction heating is different between the acicular and the regular nanomagnetite. For the regular nanomagnetite, relatively low coercivity means that the heating in a maximum induction heating field of 50 kA·m^{-1} is limited by the magnetic properties of the susceptor particles. For the higher coercivity acicular nanoparticles, the maximum heating rate is most likely determined by the thermal conductivity of the resin and/or the interfacial boundary between particles and resin.

Overall, this hysteresis verification, in conjunction with the heating data show that the susceptor particle size and shape effect on the magnetic properties make it difficult to simply ascertain the size and shape effects on heat flux via experimental methods alone. Thus, in order to fully validate the theory that heating is most constrained by heat flux between the particles and the resin, a continuation of this project into more complex modeling work is required.

CHAPTER 4:

CONCLUSIONS AND RECOMMENDATIONS

Conclusions

With the experimental configurations tested, both foam and solid SMP samples reinforced with magnetite could be activated and fully recovered on a timescale of 10-20 seconds. There was no significant impact of the nanomagnetite filler particles on the viscoelastic and thermomechanical properties of the foam, but there was a general improvement in heating performance for increased content of susceptor particles up to 10wt%.

Four analytical fitting models were evaluated for generating smoothed heating curves. The linear fit model was deemed the simplest and most useful to use for characterizing induction heating curves, until a non-empirical methodology can be found.

The initial foam experiments showed that the primary constraint in improved heating performance lies in the heat transfer between the filler nanoparticles and the foam. Subsequent experiments using solid resin with different size and shape filler powders were conducted to explore mechanisms for improving heat transfer into the SMP matrix. These experiments revealed little change due to particle size, but the results were confounded by particle clustering, and by the effect of shape on coercivity. Alignment of acicular particles prior to curing resulted in a twofold improvement in heating rate.

The sensitivity of magnetic saturation to volumetric particle content suggests that inconsistent particle loading between sample specimens is a likely source of variation in heating results. CT scans did not provide adequate resolution to characterize particle distribution below the micron level.

These findings demonstrate the viability of using particulate susceptors to actuate shape memory polymers via induction and point the way forward for performance improving material design.

Recommendations

The first recommendation for further work in this field is to investigate why the results show that reducing particle size does not significantly improve heating. As has been suggested, nanoparticle clustering may result in emulation of microparticle behavior. SEM and thermal imagery in the foam samples support this, and procedures were added into the processing of solid samples in an effort to mitigate clustering in the powders. However, the effectiveness of these procedures should be determined by re-characterizing size distribution of nanomagnetite powders after de-aggregation and in situ in the solid samples.

In order to understand the particle size and shape effect on heating, particle sizing needs to be refined and sampled at more intermediate sizes. In conjunction with this, a computational model of heat transfer should be utilized. Thermal conductivity of resin and of bulk composite samples as a function of filler content will need to be measured for use in this model. In addition to maximizing surface area of the particle-resin interface through moderating particle size, number, and shape, the bonding of the matrix to particle should also be analyzed, and improved, if warranted. Bulk heat flow improvements could also be explored experimentally by embedding carbon nanotubes.

Finally, practical application of this activation technique may warrant the use of lower current levels for human safety reasons as well as for power consumption concerns. Susceptor materials with lower coercivity may provide better heating at lower thresholds of magnetic field.

Therefore, softer magnetic materials, such as α-iron powders, should be investigated as susceptor reinforcement as well.

APPENDIX A

MAGNETISM IN MATERIALS

Magnetism

Magnetism derives from the movement of charge as discovered by Faraday and Henry in the 1830's. The theory can most easily be considered with a magnetostatic approach as diagrammed by the simple electromagnetic circuit shown in Fig. A.1. A toroid of mean path, l (here equal to 2π times the average diameter), and constant cross section, A, is the simplest magnetic circuit because the path of the circuit is uniform and the medium is continuous[27].

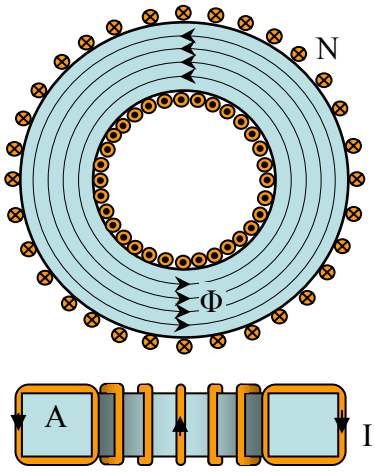

Figure A.1: Magnetic Circuit. Two cross sectional views of a simple toroidal magnetic circuit with constant cross section A. N turns of coil carry current I which orthogonally generates a homogeneous magnetic flux, Φ.

Magnetomotive force (*mmf*) gives a measure of charges moving through N turns of coil perpendicularly surrounding the magnetic circuit (eq A.1):

$$mmf = N \cdot I \tag{A.1}$$

This mmf generates a circuit of magnetic flux, Φ, orthogonal everywhere to the current. The magnitude of this flux is proportional to the *mmf* by a constant, defined as the reluctance, $\mathcal{R}$, of the circuit (eq A.2), similar to the electrical resistance term in Ohm's Law. In the same way, magnetic reluctance is dependent upon geometry and material properties embodied by *magnetic permeability*, μ (eq A.3):

$$\Phi = {mmf}/{\Re} \tag{A.2}$$

$$\Re = {\ell}/{\mu A} \tag{A.3}$$

Magnetomotive force can be normalized by path length to give the strength of an applied field, H (eq A.4). Likewise, flux can be normalized per unit of cross sectional area to give the flux density, B (eq A.5). Substitution in equations A.1-A.5 leads to the fundamental constitutive relation of magnetism (eq A.6).

$$H = {mmf}/{\ell} \tag{A.4}$$

$$B = {\Phi}/{A} \tag{A.5}$$

$$B = \mu \cdot H \tag{A.6}$$

In SI units, B (sometimes referred to as the induction field) is measured in Teslas (T) or Webers per square meter ($Wb \cdot m^{-2}$), and H works out as ampere-turns per meter ($A \cdot m^{-1}$). In free space, the flux density is dependent solely on the applied field, so the permeability term in eq A.6 becomes a conversion constant, $\mu_o = 4\pi x10^{-7}\ T \cdot A^{-1} \cdot m^{-1}$.

In the classical model of materials, atoms are envisioned as negatively charged electrons spinning and orbiting around positively charged nuclei. The electron spin and orbital motions generate magnetic dipoles. These dipoles often cancel out for most materials, but some atoms end up with a net dipole. The magnetic polarization, or aligning, of these dipoles, by an applied

field causes an additional field response generated by the material itself. This field is termed the *magnetization*, M, shown in eq A.7. In the SI system, M is measured in the same units as H.

$$B = \mu_o(H + M) \tag{A.7}$$

The magnetization is dependent upon the strength and direction of the applied field, as well as the material (eq A.8). Similar to the definition of permeability, magnetic susceptibility, χ, is defined as the proportionality constant and indeed is related (eq A.9) through substitution of eqs A.7 and A.8.

$$M = \chi H \tag{A.8}$$

$$\mu = \mu_o(1 + \chi) \tag{A.9}$$

Relative permeability, μ_r, is frequently used to describe how a material compares to free space, so that

$$\mu_r = \mu / \mu_o \tag{A.10}$$

$$\mu_r = (1 + \chi) \tag{A.11}$$

Magnetic Materials

All materials are composed of atoms and are thus magnetic, but the net magnetic response at the macroscopic level varies and can be characterized and categorized. Based upon current models and understanding, there are five classifications, which can be seen in Fig. A.2[14, 28].

1. Diamagnetic materials oppose an applied field with a small negative magnetization response. Susceptibility is typically in the range of $-10^{-4} < \chi < -10^{-9}$. Diamagnetism is a linear response that is essentially temperature independent. Most nonferrous materials (C, H_2O, etc) are classified as diamagnetic.

2. Ferrimagnetic materials contain two sublattices which respond in antiparallel directions to an applied field, but the responses are unequal, resulting in a nonlinear net positive response. Both ferrimagnets and ferromagnets are traditionally described by their relative permeability rather than susceptibility. The permeability of various ferrimagnets spans an extremely large range. The most notable ferrimagnets are spinel ferrites such as magnetite (Fe_3O_4).
3. Ferromagnetic behavior is similar to ferromagnetic, but ferromagnetic materials are usually polycrystalline alloys (such as elemental α-Fe, Ni, Co, and their alloys) containing locally uniform domains of magnetization in the lattice. The domains are already magnetized in various directions, and when a field is applied, the domains align with the applied field until saturation is achieved. The domain growth process is not entirely reversible, so like ferrimagnets, ferromagnetics are characterized by a nonlinear hysteretic response with the highest high permeability, dependent on microstructure. Both ferro- and ferri- magnets become paramagnetic above the Curie temperature, T_C. Maximum relative permeability for ferromagnetic and ferrimagnetic materials generally exceeds 100 (χ>99). Further background on ferromagnetic domain behavior and hysteresis is contained in Appendix B.

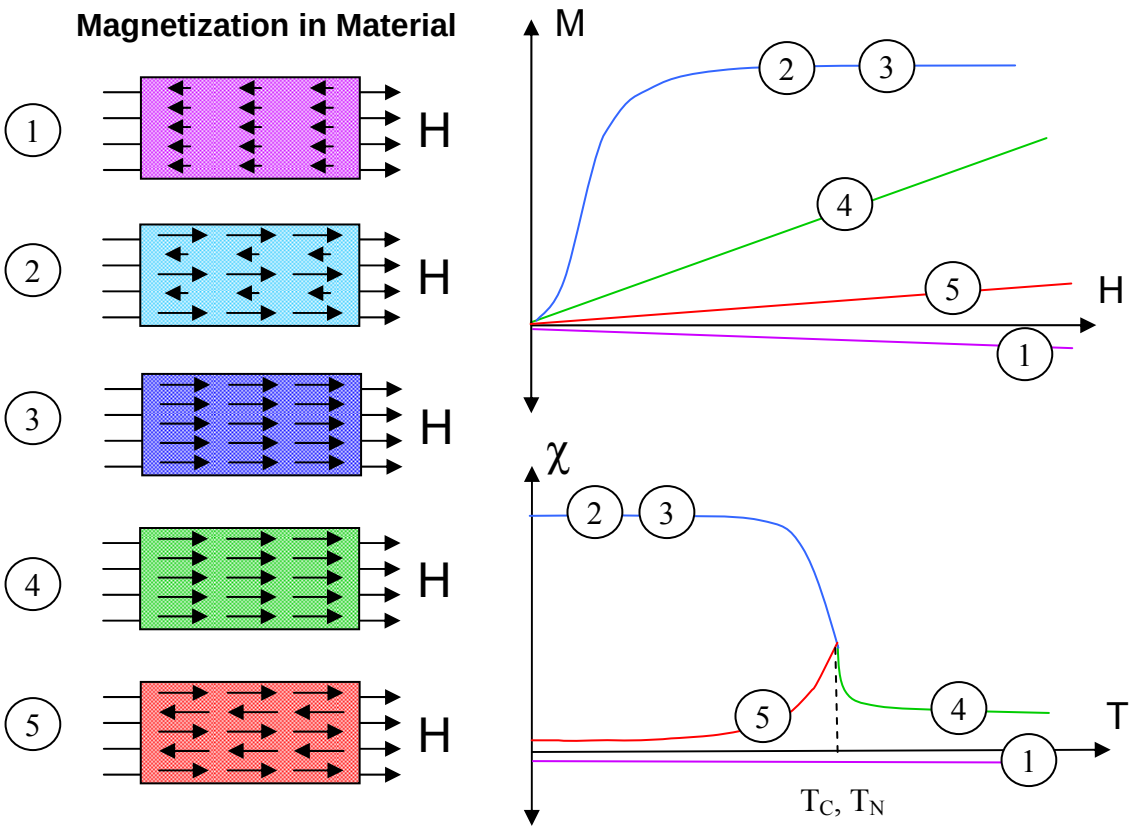

Figure A.2: Classification of Magnetic Materials. (1) *Diamagnetic* behavior is characterized by a small negative magnetization response to an applied field. This effect is generally not temperature dependent. (2) *Ferrimagnetic* materials have alternating regions of small negative response and large positive response, for a net positive nonlinear effect that is temperature dependent. (3) *Ferromagnetic* materials are characterized by a uniform alignment of magnetism and a positive nonlinear response. Both ferrimagnetic and ferromagnetic materials are characterized by hysteresis and become paramagnetic above T_c. (4) *Paramagnetic* behavior is characterized by highly positive linear response to an applied field. (5) *Antiferromagnetic* materials have alternating regions of roughly equal positive and negative response for a net effect close to zero. Above T_N, antiferromagnetic materials become paramagnetic.

4. Paramagnetic magnetic behavior consists of a linear magnetization response to an applied field. This behavior results from the random alignment and lack of interaction between magnetic moments at the atomic level, usually resulting from thermal agitation. Thus, at low temperatures (below T_C or T_N), most paramagnetic materials become ferromagnetic, ferromagnetic, or antiferromagnetic. Susceptibility is typically in the range of $1<\chi<10$, but can greatly exceed in some materials.

5. Antiferromagnetic materials are mostly rocksalts such as NiO, FeO, CoO, etc. which contain two sublattices that each respond in antiparallel directions to an applied field, largely canceling each other. There is, however, typically a small angular mismatch which results in a small net positive magnetization. Susceptibility is typically in the range of $10^{-5}<\chi<10^{-1}$. Antiferromagnetism is temperature dependent; above the Néel temperature (T_N), the material becomes paramagnetic[14, 28].

Ferromagnetism

Ferromagnetic materials are categorized as either soft or hard, depending on the shape of the magnetization curve. Hard magnetic materials exhibit a wide hysteresis curve and require a large amount of work to magnetize or demagnetize. They are useful in permanent magnets and storage media, since they retain a polarization. Soft magnetic materials exhibit a narrow hysteresis curve and require relatively little work to magnetize or demagnetize. They are useful in transformer and inductor cores, due to low hysteresis loss [28-31].

Magnetic Domains

Ferromagnetic materials contain a series of domains on the micron scale. Each domain is a uniform magnetically aligned contiguous volume. The shape of the domain may be determined by the minimization of various energies, mainly the magnetostatic, magnetocrystalline anisotropy, magnetostrictive, and domain wall energy. Each of these energies is affected by the microstructure of the material. Microstructural features such as grain boundaries, voids, and inclusions affect the energy minimization and therefore serve to define domain structure. The

entire array of domains in the material arranges itself in such a way as to minimize the total energy of the system, as illustrated in Figure A.3.

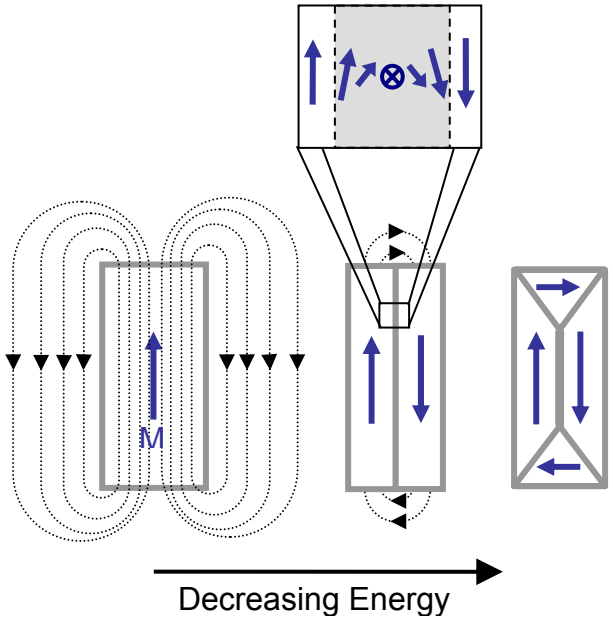

Figure A.3: Magnetic Domain Structure. Two dimensional representation of ferromagnetic domains showing how the domain structure internalizes the magnetic field, minimizing energy. The insert shows a magnified view of a 180° Bloch wall with a finite thickness. The field magnitude remains constant throughout the material, but inside the wall, the orientation transitions through a mutually orthogonal direction (into or out of the plane of the page).

Hysteresis

Magnetization in ferromagnetic materials largely consists of aligning these domains. Domain alignment is closely linked with the shape of the magnetization curve, which due to some irreversible mechanisms in the alignment of domains results in hysteresis (Fig. A.4). The initial condition of these domains without an applied magnetic field begins with a random orientation of domains. The random orientation correlates with the minimum energy configuration. As the magnetic field is increased, the growth of some domains occurs at the expense of the shrinkage of others. Eventually the domains become predominately orientated in a single direction, the preferred magnetic anisotropy direction. As the field is further increased to saturation, the domains will rotate to the applied field direction[28, 31].

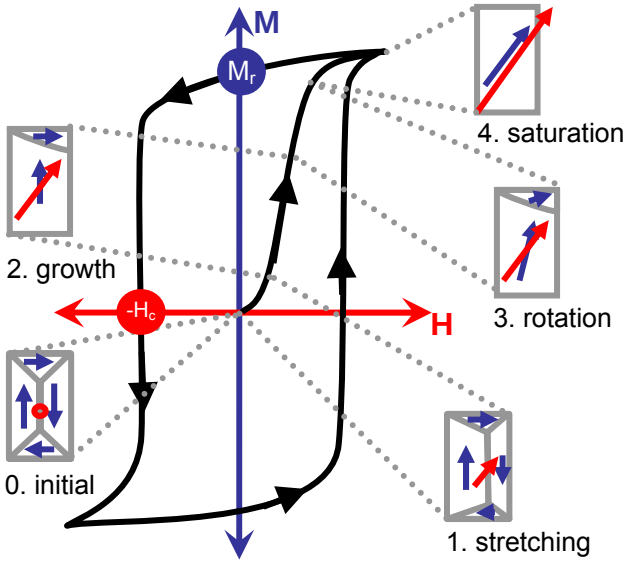

Figure A.4: Magnetic Hysteresis and Domain Alignment. Without an applied field, the natural domain structure is a combination of 90° and 180° walls (0). As a magnetic field is applied in an arbitrary direction, domains that are most favorably aligned begin to stretch (1) and grow (2), subsuming less favorably aligned regions. As the applied field continues to increase, the magnetic dipoles within each domain begin to rotate (3) into the direction of the applied field, until saturation (4). When the applied field is removed, a remanent magnetization remains (M_r). An additional reversal of applied field ($-H_c$) is required to coerce magnetization back to zero.

As the field continues to increase, the induction eventually flattens out to saturation magnetization level, M_s. If the field is then reduced back to zero and reversed, the response does not return along the original curve. A hysteresis loop is generated if the field is cycled with the arrows showing the direction of travel over the curve. The curve is called a hysteresis because, for a given a field strength, the previous magnetic history is required to know in which state of magnetization the material will be. The magnetization level after saturation when the field is reduced to zero is known as the remnant magnetization, B_r. The values of the reverse field needed after saturation to reduce the induction to zero is called the coercivity H_c. The coercivity is a measure of the *magnetic hardness*, or its ability to resist a demagnetizing field. For soft magnetic materials, such as used in inductor cores, H_c is small, but the initial susceptibility (and permeability) is high. Because of the usefulness of the induction, B, for the practical uses in inductors and permanent magnets, ferromagnetic hysteresis curves are typically shown plotted

versus B-H rather than M. This makes permeability as well as energy calculations easier to measure[32].

Demagnetizing Fields

Consider two equal cylindrical volumes of uniformly identical magnetized material, as shown in Fig.A.5. The only physical difference between the two volumes is the aspect ratio. Observation reveals that different fields, H_i, are measured at the same distance, x, from the surface of each volume. This results in different magnetization curves and thus different apparent permeabilities, μ_a.

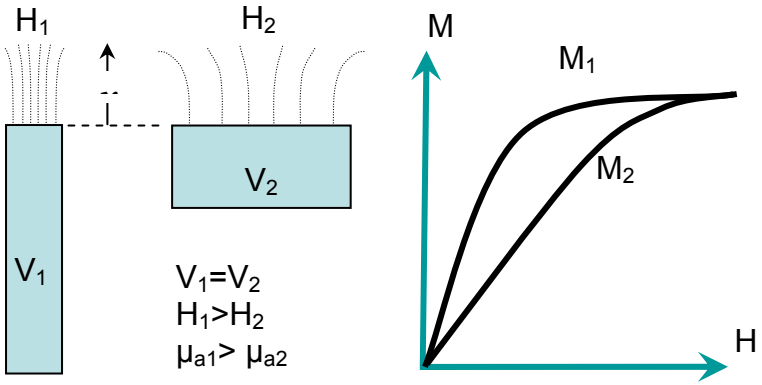

Figure A.5: Demagnetizing field effect. Two equal but different shape volumes of identical material behave differently in an applied magnetic field. Adapted from O'Handley (2000).

This phenomenon is explained in Fig.A.6. The magnetization, M, of the material, generates an additional field that contributes to what is "felt" by the sample.

$$H_i = H_a + H_d \tag{A.12}$$

This demagnetizing field, H_d, is proportional to the magnetization. N is the demagnetization factor.

$$H_d = -N \cdot M \tag{A.13}$$

N is shape and material (μ) dependent and, except for ellipsoids, varies spatially. The shape factor summed over orthogonal directions is unity, thus for spheres it is 1/3. For cubes, the

average is 1/3, but is spatially dependent. For toroids and other magnetic circuits N approaches zero in the hoop direction, but when a gap is introduced, $N>0$. If N is known, the actual permeability, μ can be calculated

$$\frac{1}{\mu} = \frac{1}{\mu_a} - N \tag{A.14}$$

where $\mu_a = B/H_a$ is the apparent permeability.

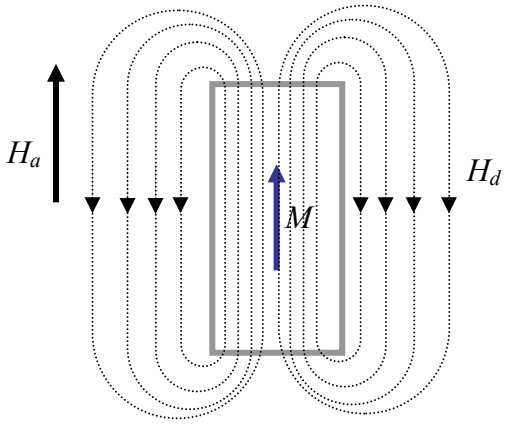

Figure A.6: Explanation of demagnetizing field. Magnetization of the volume via an applied field (H_a) creates a field loop joining the two surface poles. Some of this opposing field passes back through the material, acting as a demagnetizing force (H_d). The total internal field in the material is the sum of the applied field and the demagnetizing field.

References

1. Sokolowski, W.M., S. Hayashi, and T. Yamada, eds. *Cold hibernated elastic memory (CHEM) self-deployable structures*. Smart Structures and Materials 1999: Electroactive Polymer Actuators and Devices. 1999, SPIE.

2. Tey, S., W. Huang, and W. Sokolowski, *Influence of long-term storage in cold hibernation on strain recovery and recovery stress of polyurethane shape memory polymer foam.* Smart Materials & Structures, 2001. **10**: p. 321-325.

3. Tobushi, H., et al., *The influence of shape-holding conditions on shape recovery of polyurethane-shape memory polymer foams.* Smart Materials & Structures, 2004. **13**.

4. Tobushi, H., et al., *Thermomechanical properties of polyurethane shape-memory polymer foam.* Shape Memory Materials and Its Applications, 2001. **394**(3).

5. Incropera, F.P. and D.P. De Witt, *Introduction to Heat Transfer*. 1990, New York: John Wiley & Sons.

6. Buckley, P., et al., *Inductively Heated Shape Memory Polymer for the Magnetic Actuation of Medical Devices.* IEEE Transactions on Biomedical Engineering, 2005.

7. Ken Gall, et al., *Thermomechanics of the shape memory effect in polymers for biomedical applications.* Journal of Biomedical Materials Research Part A, 2005. **73A**(3): p. 339-348.

8. Yakacki, C.M., et al., *Unconstrained recovery characterization of shape-memory polymer networks for cardiovascular applications.* Biomaterials, 2007. **28**(14): p. 2255-2263.

9. Beblo, R. and L.M. Weiland, *Light Activated Shape Memory Polymer Characterization Challenges and Strategies*, in *39th ISTC*. 2007, SAMPE: Cincinnati, OH.

10. Annette, M.S., *Electromagnetic Activation of Shape Memory Polymer Networks Containing Magnetic Nanoparticles.* Macromolecular Rapid Communications, 2006. **27**(14): p. 1168-1172.

11. Di Prima, M.A., et al., *Thermo-mechanical behavior of epoxy shape memory polymer foams.* Smart Materials & Structures, 2007. **16**: p. 2330-2340.

12. Sanderson, T. and K. Gall, *Shape Memory Polymer Characterization for Advanced Air Vehicle Technologies.* Raytheon Technology Today, 2007(4): p. 10.

13. Lendlein, A. and S. Kelch, *Shape-Memory Polymers.* Angewandte Chemie International Edition, 2002. **41**(12): p. 2034-2057.

14. Benenson, W., et al., *Handbook of Physics*. 2006, New York: Springer.

15. Metaxas, A.C., *Foundations of Electroheat: a Unified Approach*. 1996, Chichester: John Wiley & Sons.

16. Haimbaugh, R.E., *Practical Induction Heat Treating*. 2001, Materials Park, Ohio: ASM International 332.

17. McHenry, M., M. Willard, and D. Laughlin, *Amorphous and nanocrystalline materials for applications as soft magnets.* Progress in Materials Science, 1999. **44**(4): p. 291-433.

18. Suwanwatana, W., S. Yarlagadda, and J.J.W. Gillespie, *Influence of particle size on hysteresis heating behavior of nickel particulate polymer films.* Composites Science and Technology, 2006. **66**(15): p. 2825-2836.

19. Razzaq, M.Y., et al., *Mechanical Spectroscopy of Magnetite Filled Polyurethane Shape Memory Polymers.* Materials Science and Engineering A, 2007. **471**: p. 57-62.

20. Razzaq, M.Y., et al., *Thermal, electrical and magnetic studies of magnetite filled polyurethane shape memory polymers.* Materials Science and Engineering: A, 2007. **444**(1-2): p. 227-235.

21. Tobushi, H., et al., *Thermomechanical properties in a thin film of shape memory polymer of polyurethane series.* Smart Materials & Structures, 1996. **5**(4): p. 483-491.

22. Koerner, H., et al., *Remotely actuated polymer nanocomposites—stress-recovery of carbon-nanotube-filled thermoplastic elastomers.* Nature Materials, 2003. **3**: p. 115-120.

23. Arzberger, S.C., et al. *Elastic Memory Composites (EMC) for Deployable Industrial and Commercial Applications*. in *Smart Structures and Materials 2005: Industrial and Commercial Applications of Smart Structures Technologies*. 2005: SPIE.

24. Gross, K. and L. Weiland. *Flexural testing of shape memory polymers for morphing aircraft applications*. 2008. Seattle, WA, United States: American Society of Mechanical Engineers, New York, NY 10016-5990, United States.

25. Liu, Y., et al., *Thermomechanics of shape memory polymers: Uniaxial experiments and constitutive modeling.* International Journal of Plasticity, 2006. **22**: p. 279-313.

26. Sanderson, T., et al., *Thermal Properties of an Open Cell Epoxy Shape Memory Polymer Foam* in *SAMPE Fall Technical Conference and Exhibition*. 2007: Cincinnati, OH.

27. Karapetoff, V., *The Magnetic Circuit*. 2006: Merchant Books.

28. O'Handley, R.C., *Modern Magnetic Materials*. 2000, New York: John Wiley and Sons, Inc.

29. Bozorth, R.M., *Ferromagnetism*. 1951, Toronto/NewYork/London: D. Van Nostrand Company, Inc.

30. Bozorth, R.M., et al., *Magnetic Properties of Metals and Alloys*, in *National Metal Congress and Exposition*. 1959, ASM: Cleveland, Ohio.

31. Jiles, D.C. and A. D.L., *Theory of Ferromagnetic Hysteresis.* Journal of Magnetism and Magnetic Materials 1986(61): p. 48-60.

32. Cullity, B.D., *Introduction to Magnetic Materials*. 1972, Reading, Massachusetts: Addison-Wesley Publishing Company.